FRONT MATTER

- **Title: An Isoperimetric Soft Robot: A constant edge-length robotic truss capable of dramatic shape change and untethered operation**
- **Short Title: A Soft, Untethered, Isoperimetric Robot**

Authors

Nathan S. Usevitch[1,*,‡], Zachary M. Hammond[1,*,‡], Mac Schwager[2], Allison M. Okamura[1], Elliot W. Hawkes[3,†], Sean Follmer[1,†]

[1]Department of Mechanical Engineering, Stanford University
[2]Department of Aeronautics and Astronautics, Stanford University
[3]Department of Mechanical Engineering, University of California, Santa Barbara
[*]These authors contributed equally to this work.
[†]These authors contributed equally to this work.
[‡]Corresponding Author: usevitch@stanford.edu

Abstract

In many real-world applications, robots must be human-safe, untethered, and adaptable. Toward these goals, we propose an untethered, inflated robotic truss, composed of thin-walled inflatable tubes, that demonstrates dramatic shape change by continuously relocating its joints while its total edge-length remains constant. We term this "isoperimetric." Specifically, a set of identical roller modules each pinch the tube to create an effective joint that separates two edges, and modules can be connected to form complex structures. Driving a roller module along a tube changes the overall shape, lengthening one edge and shortening another while the total edge-length and hence fluid volume remain constant. This isoperimetric behavior allows the robot to operate without compressing air or requiring a tether. Our concept brings together advantages from three distinct types of robots–soft, collective, and truss-based–while overcoming certain limitations of each. Our robots are robust and safe like soft robots but not limited by a tether; are modular like collective robots but not limited by complex subunits; and are shape-changing like truss robots but not limited by rigid linear actuators. We demonstrate 2D robots capable of dramatic shape change and a human-scale 3D robot capable of punctuated rolling locomotion and manipulation, all constructed with the same modular rollers and operating without a tether. We analyze the compliance of these robots, discuss how the kinematics of isoperimetric robots differ from conventional truss robots, and characterize the roller modules. Our concept advances the vision of human-safe, untethered, and adaptable robots interacting in the real world.

Summary

A large-scale, isoperimetric, untethered, soft robot changes shape by manipulating constant-length inflated tubes via movable joints.

MAIN TEXT

Introduction

For robots to work in conjunction with humans and be useful outside of highly engineered environments they must be human-safe, robust, adaptable to a variety of scenarios, and capable of moving through diverse types of terrain. These attributes not only require adaptable control algorithms and the collection and processing of rich sensory information, but also new forms of reconfigurable, adaptable robotic structures, potentially soft in nature.

In this work, we present a concept for such a robotic structure: a truss of inextensible, inflatable, constant-length tubes that are manipulated by a collective of interconnected roller modules, allowing for shape change and compliance without a pressure source (Fig. 1A). Pressurized tubes serve as structural elements and the edges of the truss. Each joint in the tubing is formed by a robotic roller module which pinches the tube between cylindrical rollers without creating a seal. The roller modules can be connected to neighboring modules to form a node of a complex 2D or 3D structure. An electric motor and mechanical transmission then drive these rollers like wheels along the tube, causing the pinch point to translate (Fig. 1B). Edge lengths of the robot are changed not by stretching or contracting the edges, but by movement of the roller module along the tube—moving the effective joint and simultaneously lengthening one edge while shortening another (Fig. 1C and Movie S1). The sum of all the edge lengths remains constant, therefore we call the robot an isoperimetric system (constant perimeter). A gap between the rollers ensures that as they move, there is negligible pressure difference between the two edges, leading to a system with constant volume that does not require a pressure source. The individual roller modules are simple, capable of moving along the tube in only one degree of freedom, yet the overall collective is capable of complex behavior.

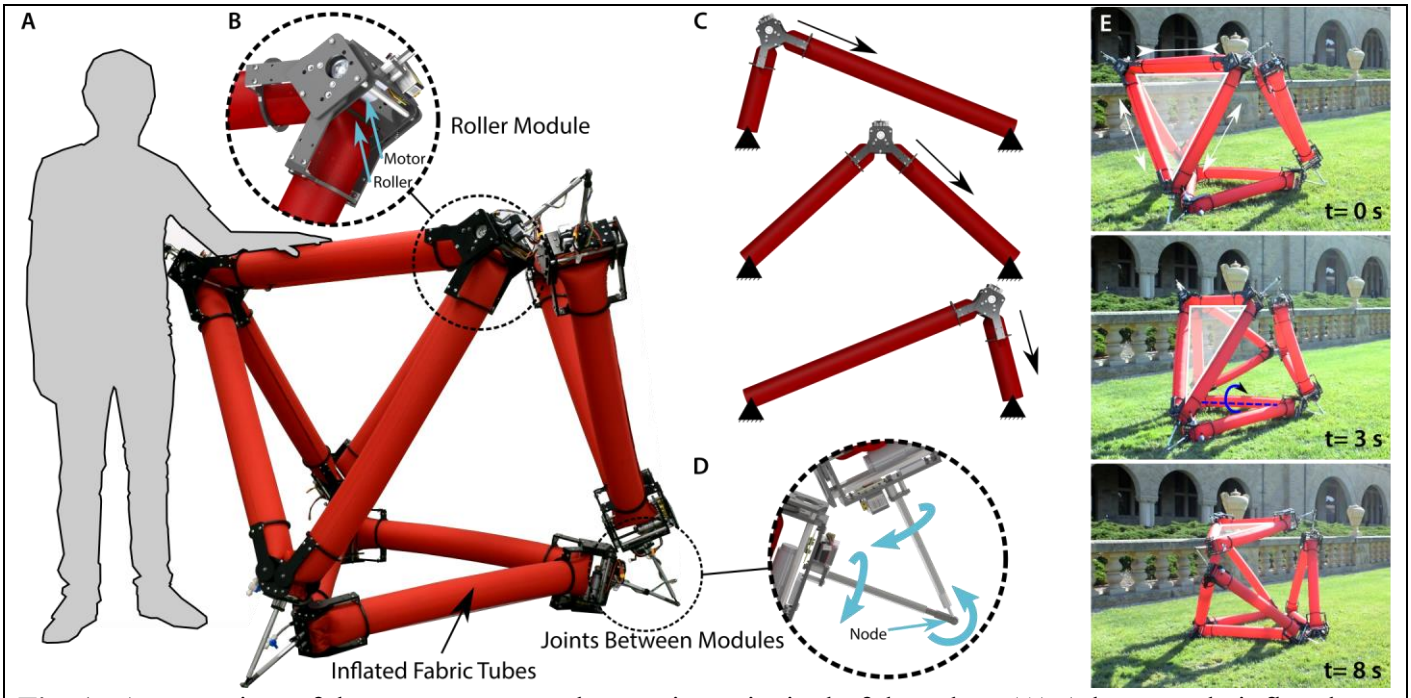

Fig. 1. An overview of the components and operating principal of the robot. **(A)** A large-scale inflated robot that does not require a tether. The robot is composed of a set of identical robotic roller modules that are mounted onto inflated fabric tubes that form the primary structure of the robot. **(B)** The rollers pinch the fabric tube between roller, creating an effective joint which can be relocated by driving the rollers. **(C)** The roller modules actuate the robot by driving along the tube, simultaneously lengthening one edge while shortening another. The roller modules can connect to one another to construct two- and three-dimensional truss-like structures capable of shape change and locomotion. **(D)** The roller modules connect to each other at nodes using three-degree-of-freedom universal joints that are comprised of a clevis joint that couples two rods, each free to spin about its axis. The arrows indicate how the joints can rotate. **(E)** The robot locomotes untethered outdoors using a punctuated rolling gait. One face of the robot is highlighted to illustrate the rolling motion.

Our robotic concept is built upon a synthesis of concepts from collective, truss, and soft robots. This allows us to realize a unique set of traits, as we exploit advantages while bypassing certain disadvantages of each individual type of robot.

As a collective system of robots, our concept is inherently modular with interchangeable, simple (one-degree-of-freedom) subunit roller modules. However, because our subunits are physically interconnected through a compliant network, the collective achieves complex system-level behavior, capable of applying forces in three dimensions to the human-scale world. This overcomes a limitation of collective robots that combine together to create structures that can change their shape (*1-4*)—realizing complex 3D physical interaction while maintaining simplicity at the individual robot level. A related type of collective robotic system employs teams of robots that build passive structures *(5-8).* The target structure is often truss-like, built by adding passive elements, and sometimes requires that the robots traverse the structure as they build it. As opposed to discretely rearranging passive elements within a structure to change its shape, in our concept the collective continuously deforms passive bodies to change the locations of where the bodies are attached, resulting in very simple robotic subunits.

As a truss-like robot—which have been proposed for intriguing applications like exploring planets (*9-12*), burrowing underground (*13*), shoring up rubble (*14,16*), and modular robotic systems (*17,18*)—our concept is adaptable and customizable. However, because our robot has a compliant structure and moves without requiring linear actuators, it affords robustness that is lacking in other truss-like robots. Ideally, the linear

actuators of a truss robot would be lightweight, robust, have a high extension ratio, and operate untethered. While certain new actuators meet some of these requirements (*19-22*), achieving all is challenging. This means that when existing actuators are connected into a truss system, the resulting robot is relatively rigid, slow, heavy, and lacking in robustness to large impacts. Our robot overcomes some of the challenges of conventional truss robots because the structure is composed of lightweight compliant pneumatic beams. Tensegrity robots also overcome the fragility of truss robots, but through a network of compliant cables or compliant beams that create part of their structure (*23-28*). Tensegrity robots can undergo large shape change, especially volume change for deployment, but the fact that typically only a subset of edges change length, and some edges may only support tensile loads, imposes some constraints on the possible shape change. Our robot is not a tensegrity robot, but it incorporates the compliant characteristics that have made tensegrity robots more robust, in order to enable tough robots that are highly adaptable.

As a soft robot, our concept is inherently human-safe and has a high tolerance to uncertainty in the environment (*29-33*). However, because it is a constant-volume, isoperimetric system (nodes move, but the total length of the pneumatic structure remains the same), it overcomes a fundamental limitation of pneumatic soft robots—the air supply. Previous methods to provide pneumatic power onboard include carrying a micro-compressor (*34*, *35*), carrying a pressurized fluid reservoir (*36*), utilizing chemical decomposition (*37*), and using explosive fuels (*38,39*). However, each of these is limited: micro-compressors have low flow rates and peak pressures, compressed air in a reservoir has limited overall capacity, chemical decomposition or burning of a fuel often requires systems level integration and does not easily provide air at useful pressures and rates (*40*). In contrast, other soft systems use a fixed amount of air within a cavity as a structural element and not as an actuator, requiring no pressure source once the cavity is pressurized (*41-46*). Interestingly, some of this work has exhibited direct manipulation of the membrane of an inflated beam to create bending without compressing the air within (*42,43*). We build upon this work for our soft, untethered robot but instead of manipulating a serial robot by deforming the membrane around fixed joints as in (*42,43*), we continuously move the effective joints along the structure which allows for large global shape-change of a truss-like robot.

In the remainder of this paper, first, we present demonstrations and characterizations of the collective, truss-like, and soft nature of our robots. To highlight the collective and modular nature of the robot, we present three different robots, two 2D robots and one 3D robot, each constructed from identical one-degree-of-freedom roller modules, yet as a collective, capable of complex movement. To demonstrate the truss-like nature of the robot, we show dramatic shape change of all three of the robots and punctuated rolling locomotion of the 3D robot. To demonstrate and characterize the softness of the robot, we show its robustness to crushing forces, measure its behavior under load, and leverage its compliance to grasp and manipulate objects. Each of these demonstrations is conducted with the robot untethered from a pressure source. Second, we present the models and experiments that inform the mechanical design of the subcomponents of the robots. Third, we provide insights into the tradeoffs among our robots, truss robots, and pneumatically actuated robots through theoretical analysis of reachable workspace, efficiency, and speed. Finally, we discuss the implications of our results.

Results

Demonstration and Characterization of Collective, Truss-like, and Soft Nature of the Robot

2D Collective Demonstrating Truss-like Shape Change

We demonstrate the collective and modular nature of the isoperimetric concept by constructing two different 2D robots with the same roller modules (Fig. 2). The first robot is composed of three separate tubes and the

second of a single tube. Robots with multiple tubes are interesting because the modularity is extended to robotic substructures containing multiple roller modules. For example, substructures designed for specific tasks like grasping or locomotion could be combined to form a variety of robots. On the other hand, robots with a single tube have fewer constraints on their configuration and larger maximum edge lengths. With both robots, we demonstrate a truss-like shape changing ability.

For the first robot, each of the three individual tubes (3.4 m long and 0.1 m diameter) is routed through two active roller modules before affixing its ends to a passive module which does not contain a motor, creating a triangle. The triangular substructures are then assembled by connecting pairs of roller modules with revolute joints, showing that complex robots can be assembled from multiple simpler robots. The robot can deploy from a small area of $0.85\ m^2$ without human intervention when air is added from an external source (Fig. 2A). After the robot is inflated to an operating pressure of 40 kPa (and an area of $2.9\ m^2$), we remove the tether and drive the roller modules to demonstrate a few feasible shapes: a tall skinny triangle, a hexagon, a square, and a "pincer" shape that can grasp an object (Fig. 2B). It takes less than 50 seconds for the robot to transition among all four of these shapes (Movie S2). The minimum length of an edge is 28 cm for this prototype and is fixed by the size of the roller module.

For the second robot, we route a single tube with a length of 6.8 m through 8 active roller modules and a single passive module, as shown in Fig. 2C and Movie S3. This single-tube architecture enables certain behaviors that are not possible with the first, three-triangle architecture, where an edge can only lengthen if another edge in the same triangle shortens. In contrast, when a single tube is used for the entire robot, the material can be exchanged between any two edges in the network. To exchange length between edges that are adjacent, one roller module moves along the tube (Fig. 2D). For edges that are not adjacent, all intermediate powered roller modules must roll to transfer the tube material, even if the edges adjacent to the intermediate roller modules do not change length (Fig. 2E). Because any edge in the robot can contribute length to any other edge, much larger maximum edge lengths can be reached with the single tube architecture (Fig. 2F), illustrating that the maximum length of an edge depends on the robot architecture.

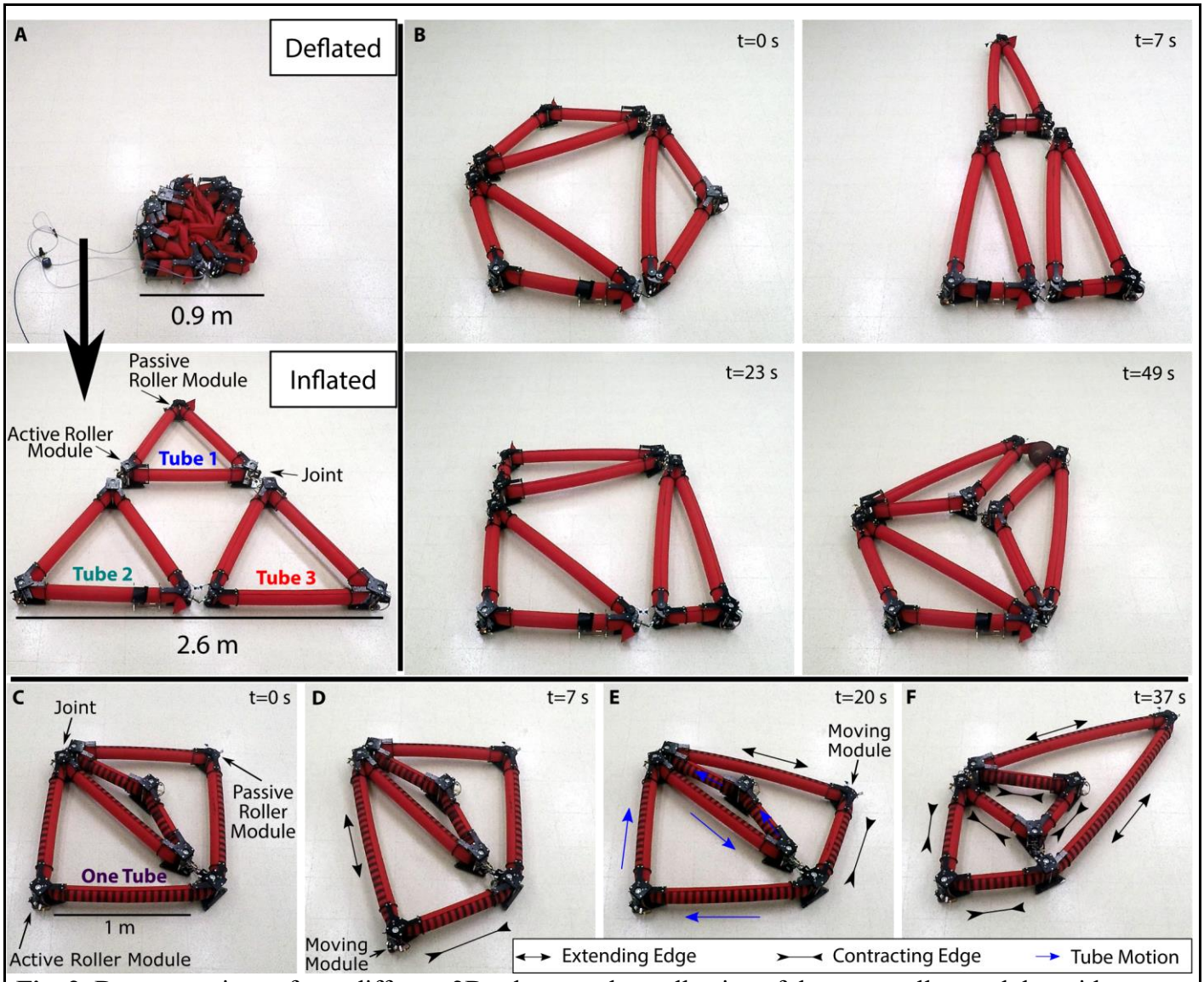

Fig. 2. Demonstrations of two different 2D robots, each a collective of the same roller modules with different tube architectures, showing truss-like shape change. **(A)** A robot, formed from three separate tubes that are routed into triangles and connected together, inflates and springs into shape without intervention. **(B)** This three-tube robot can change to a variety of shapes. Casters under the roller modules allow motion. **(C)** A robot composed of a single inflated tube. It can more dramatically lengthen its edges, because each edge can exchange material with any other edge. The single tube design also means that sometimes roller modules must run to pass material through the network, even if the edge lengths immediately connected to it are not changing length. **(D)** A single active roller module moves causing one adjacent edge to shorten and the other to lengthen. **(E)** To lengthen and shorten the two edges adjacent to the passive module, all of the active roller modules move in coordination. **(F)** The single tube configuration is capable of much larger edge lengths because all other edges can shorten to accommodate the lengthening of two edges.

3D Octahedron Robot: Truss-like Shape Change and Locomotion

We use the same roller modules from the 2D robots to create a 3D octahedron, formed by connecting 4 individual triangles, each with a tube length of 3.4 m. As before, a triangle has two active and one passive modules. We demonstrate truss-like 3D shape-changing and locomotion.

The first demonstration of the 3D robot explores its volume change during deployment (Fig. 3A). The structure can compact to a volume of 0.173 m^3 when deflated (fitting within a 64 x 71 x 38 cm rectangular prism), and then deploy to an octahedron with a volume 2.29 m^3, increasing by a factor of 13. Next, after untethering the robot, we show it is capable of dramatically changing its shape, including changing its height by a factor of two and moving to an asymmetric configuration where one node extends upwards (Fig. 3B, Movie S4). Movie S5 shows a simulated robot moving according to our kinematic model (Materials and Methods) side-by-side with the real robot moving. While not a perfect agreement, the character of the robot motion is captured by the simulation. Small errors develop due to imperfections in our current fabrication methods leading to variations in tube diameter and length. Finally, we demonstrate locomotion. The robot can locomote with a punctuated rolling gait at a speed of 2.14 body lengths per minute, or 3.6 m/min (Fig. 3C and Movie S6). In the current implementation, each roller module has a battery life of about 23 minutes under continuous roller movement (see S1 for more information).

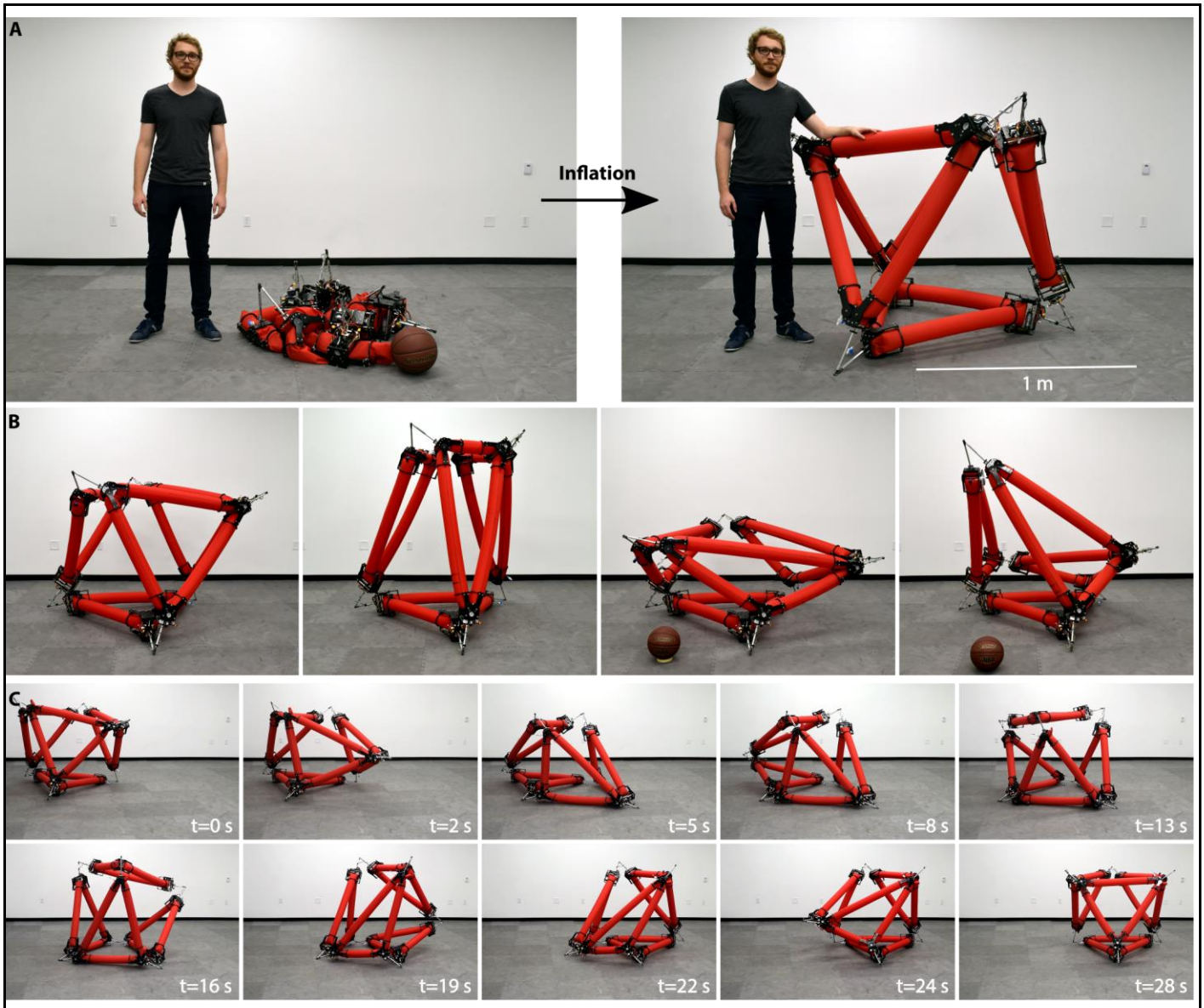

Fig. 3. A 3D untethered, octahedron truss robot capable of shape-morphing and locomotion. **(A)** The robot first inflates from a small package into an octahedron. The octahedron is composed of 4 individual triangles. **(B)** The robot can exhibit extreme shape change. A 186 cm height human and a 24 cm-diameter basketball are shown for size reference in some images. **(C)** The robot is also capable of a punctuated rolling gait, beginning with one of the four triangles as a bottom face (first photo) and returning to this

configuration (with a different triangle now at the bottom) after two rolling events (last photo).

3D Octahedron Robot: Compliant Behavior and Manipulation

The inflated fabric tubes are compliant, a hallmark of soft robots and a property that affords robustness to the structure. To demonstrate this robustness (Fig. 4A and Movie S7), we load the robot with a wooden pallet before increasing the load until structural failure (Fig. 4A). When the load is removed and external forces are applied to restore the structure to its initial shape, it is again able to support the initial load, undamaged. To quantify the response of the robot under load, we measure force while displacing the top roller module of a single triangle in three different configurations using the experimental setup described in Supplementary Text and Fig. S5. The results are shown in Fig. 4B. When an external load is applied to a node of the truss structure, there is a relatively high initial stiffness until the load causes one of the beams to buckle, at which point the force exerted at the node dramatically decreases, approaching a zero-stiffness regime. This behavior is like a mechanical fuse: during normal operation, the structure is relatively stiff, allowing functionality; yet beyond some threshold force, it buckles, limiting damage to itself or the environment. The exact level of the threshold force could be tuned via control of the robot configuration, leveraging existing work on the mechanics of inflated beams (*47-49*). Because of its relatively high stiffness before buckling, the robot can carry heavy loads without significant deformation. Fig. 4C and Movie S8 demonstrate the robot moving a 6.8 kg load over a trajectory. The kinematics model also allows us to predict the forces experienced by the members. Movie S9 shows the predicted axial load on each inflated member while it changes shape in the presence of an external load similar to the experiment in Fig. 4C.

Different recovery strategies can be invoked after an inflated beam buckles. Occasionally, the beam will recover on its own when the load is removed. This is due to the small but noticeable restoring forces seen in Fig. 4B. If a beam is unable to recover passively, it is possible for active motions of the roller modules to assist in straightening buckled beams (Movie S10).

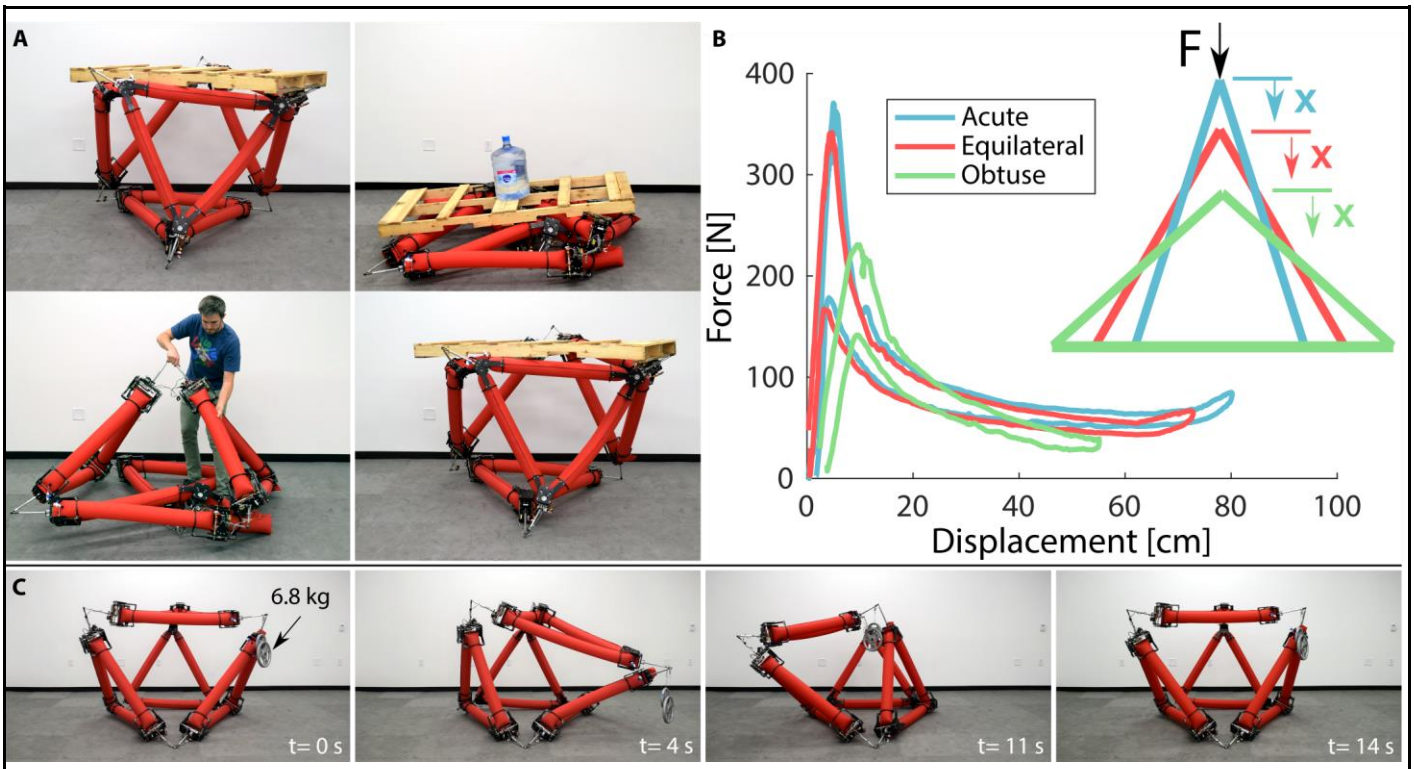

Fig. 4. Demonstration and characterization of the robot's compliant behavior. **(A)** Overloading the robot causes the robot to collapse. After being restored to its initial configuration, the robot is again able to

support the initial load. **(B)** The load displacement behavior of a single triangle in three different configurations. In all cases, there is a moderate initial stiffness until a critical load is reached and the beam buckles, at which point the force required to maintain a given level of deflection is much lower than the peak value, demonstrating a mechanical-fuse-type behavior of the robot. **(C)** The robot moves a 6.8 kg load over a trajectory.

The compliance of the robot allows it to grasp and manipulate objects. We demonstrate this behavior in Fig. 5A, as the robot changes shape to engulf an object (a basketball) before changing shape to pinch the object between two of its edges. The compliant beams bend slightly around the object, increasing the contact area. Once the object is grasped, it changes the shapes of its other faces to pick the object up from the ground. The robot can also manipulate objects "in-hand," leveraging the fact that the edges are composed of continuous tubes that move relative to the nodes. In Fig. 5B, a basketball is placed between two edges of a tube. By driving the roller module closest to the basketball, the tube moves relative to the basketball, causing the ball to rotate within the grasp (Movie S11).

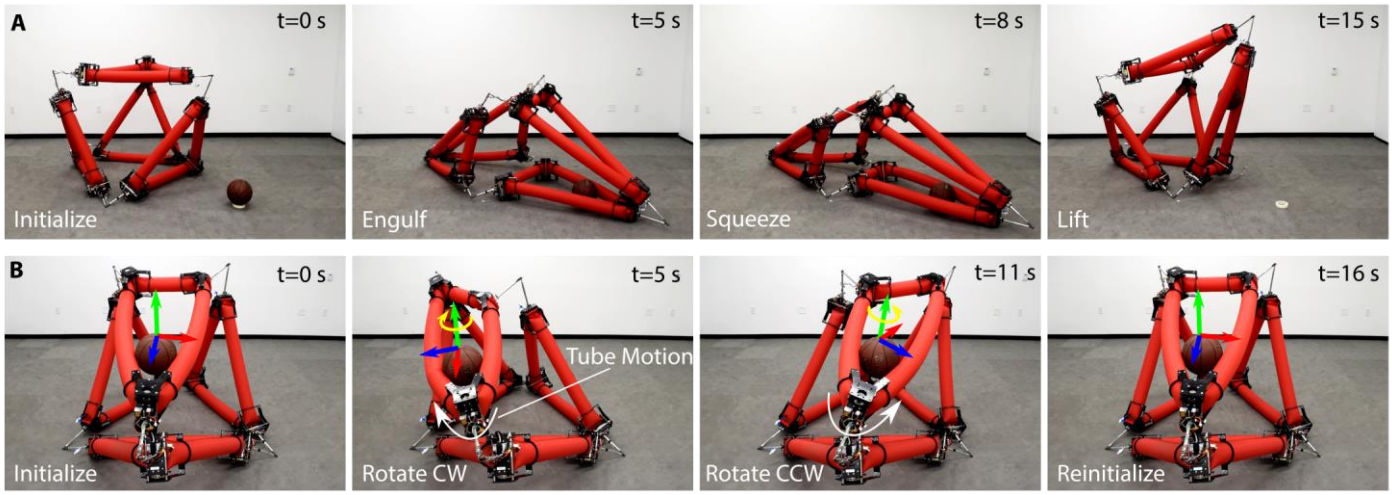

Fig. 5. Demonstration of the robot's ability to use its inherent compliance to manipulate and interact with objects. **(A)** The robot grasps a basketball (diameter of 24 cm, mass of 580 g) by first engulfing it, and then pinching it between two compliant edges. The robot then change shape to lift the basketball into the air. **(B)** With the basketball secured between two edges, motion of the roller module closest to the basketball cause the basketball to spin. A coordinate frame has been added to allow visualization of how the orientation of the basketball changes. Between the second and third configurations the basketball rotates approximately 135 degrees.

Robot subcomponent analysis and design

The key components of our robot are the tubes and the actuated roller modules, shown in Fig. 1. Each roller module in the robot serves three primary functions: (i) to pinch the tube, creating a region of low bending stiffness—an effective joint, (ii) to locomote along the length of the tube, moving the position of the effective joint, and (iii) to mechanically couple to other roller modules in the structure in a way that fully defines the geometry of the robot. In this section we review the analysis and design to support those three primary functions.

Joint-like Behavior of a Pinched Tube

The effective joints, about which two sections of tube pivot, are created by the cylindrical rollers in the roller modules. The rollers pinch the tube, reducing its cross-sectional area and bending stiffness while still

allowing airflow. Ideally, there would be no torque required to change the angle, but in practice there is a torque at these joints. To understand and minimize this torque, we developed a reduced order model. We assume the fabric that makes up the pressurized tube is flexible yet inextensible, and takes a shape that maximizes the enclosed volume, independent of its material properties or internal pressure. We relate the torque applied by the joint $\left(\tau(\theta)\right)$ to the internal pressure P and the change in volume with angle $\left(\frac{dV(\theta)}{d\theta}\right)$ using the principle of virtual work through $\tau(\theta) = P\frac{dV(\theta)}{d\theta}$. See Supplementary Text and Fig. S2.

To validate the model, we gather data using the test setup presented in Fig. S2C and compare it with predictions from the model (Fig. 6). The data show that at small angles, torque increases with roller diameter (Fig. 6A) and tube diameter (Fig. 6B). At a certain angle, the two sections of tube collide with one another and the torque increases rapidly, as illustrated in Fig. 6A. We terminate the predictions at the onset of this interference, which occurs at a larger angle with increased roller diameter, and a smaller angle with increased tube diameter. The model captures the shape of the curve until interference occurs, although it slightly underpredicts the resulting force. This could be because it accounts only for the response of the air, and not for the resistance of the fabric tube to bending.

Examining the trends from Figs. 6A and 6B, it is ideal to use small rollers to reduce the torque associated with the tubes pivoting about the effective joint but use large rollers to avoid the self-interference of the tube. To address these competing objectives, we introduce a design that utilizes two pairs of rollers as shown in Fig. 6C. In this way, we gain the low-torque performance of the small rollers while also avoiding the self-interference that drastically increases torque (Fig. 6D).

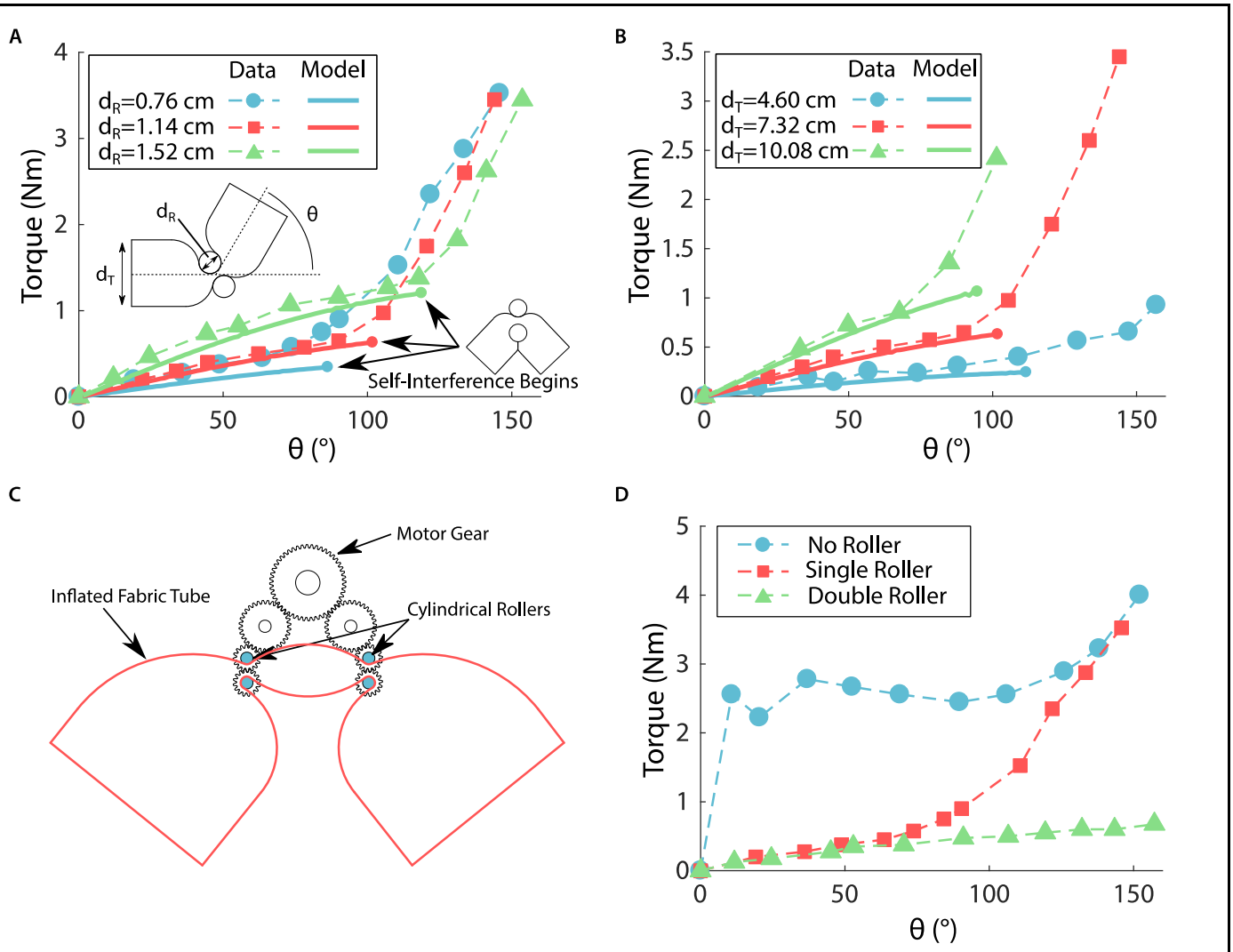

Fig. 6. Analysis of the effective joint formed by rollers pinching a tube. (**A**) The relationship between angle and torque with changing roller diameter (tube diameter is 7.32 cm). Model predictions are shown in solid lines and experimental data in dashed lines. The model slightly underpredicts the torque. The amount of torque increases substantially beyond the point where the model predicts self-interference. Torque increases with roller size, but interference also begins at larger angles. **(B)** Increasing torque with increasing tube diameters when the roller diameter is 1.14 cm. **(C)** The double roller configuration and the gear train that ensures all rollers move together from a single motor input. **(D)** The torque required to bend a tube with no rollers, with a single set of rollers, and with two sets of rollers as shown in (C) (roller diameters are 0.64 cm separated by 6.35 cm). Without rollers, the tube exhibits low stiffness, but large torque at a wide range of angles. The presence of one set of rollers dramatically reduces the torque at low angles but the torque rises quickly after self-interference begins. With two sets of rollers the torque is low for small and large angles because the tube does not self-interfere.

Locomotion along an Inflated Tube

The second requirement of the roller module is to continuously move the joint along the structure, which it does by rotating the rollers with a motor. Because the gap between the rollers is smaller than the diameter of the tube, the rollers experience a high normal force pushing them apart (see Supplementary Text and Fig. S3 for further analysis). This, when coupled with a high-friction coating on the cylinders, ensures a large friction force between the tube and the rollers and prevents slip.

In an ideal case, the energetic cost to move the roller along the tube would be zero and invariant to changes in the internal pressure of the system. However, the presence of friction and hysteresis in the deformation of the fabric results in an energetic cost to travel a distance, which we seek to minimize.

To measure the cost to move in the presence of the non-idealities, we use the experimental setup presented in Supplementary Text and Fig. S4. The first test examines the effect of roller diameter and internal pressure on the force required to move tubes through a pair of rollers where the tube has a diameter of 7.32 cm. We find a linear relationship between force and pressure (Fig. 7A). The diameter of the roller has a small effect on the slope of these lines with the largest rollers having the largest slope.

In the second test, we measure the effects that the internal pressure and tube diameter have on the force required to move tubes through a pair of rollers 1.14 cm in diameter. We observe that increases in pressure and tube diameter both increase the force to move (Fig. 7B). This is because both factors result in a larger normal force on the rollers, and a larger diameter tube results in more material being deformed through a larger motion.

In the third test, we compare the cost to move of a single set of rollers to that of two pairs of rollers separated by a variable distance. In Fig. 7C, we show that the cost to move for two pairs of rollers is less than twice that for one roller. Note that we tested roller spacings less than a diameter of the tube because spacing greater than a diameter is not effective at reducing joint torque and is thus not practical.

To gain a sense of the relative magnitude of the forces required to move the tube through the rollers, we compare the measured force with the maximum force that could be exerted by the pressurized air, calculated as pressure times the cross-sectional area of the tube. Across all of the data presented in Fig. 7, the forces required to move the tube through the rollers has a peak of 14.6% and a mean of 8.78% of the maximum force, indicating that the forces required to move the tube through the rollers are small in comparison.

Having examined the geometric effects on joint stiffness and the cost to move, we can make some design decisions. Using smaller rollers reduces the joint stiffness (Fig. 6A) and decreases the cost to move (Fig. 7A). Therefore, using small rollers is preferable for performance. Increasing the spacing between the pairs of rollers decreases the minimum angle before tube interference but also increases the cost to move. For our roller modules, we select a roller diameter of 0.76 cm and set the distance between the center axis of the rollers at 1.27 cm. The distance between the two pairs of rollers is 6.35 cm. In practice, we drive both sets of rollers with a single motor through the gear train shown in Fig. 6C.

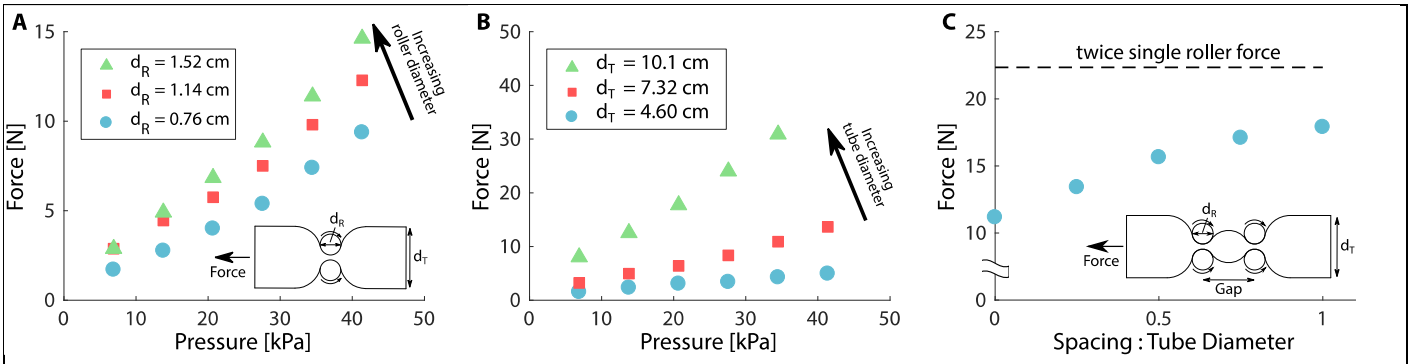

Fig. 7. Exploration of the energetic cost to move along the tube. (**A**) The force required to move the tube through the rollers over a range of pressures and with three different roller diameters. Tube diameter is 7.32 cm. The force-pressure relationship is approximately linear and increasing the roller diameter slightly increase the required force. (**B**) The force required to move the tube through the rollers over a range of pressures and with three different tube sizes. Roller diameter is 1.14 cm. The force-pressure relationship is

approximately linear, and tubes with larger diameter require more force. (**C**) The force required to move a 10.1 cm tube at 30 kPa through two pairs of 0.76 cm rollers over a range of distances between the pairs. A single roller is included with gap distance equal to zero. The double roller cost to move when the separation is equal to the tube diameter is 80% of twice the single roller cost to move.

Roller Connections

The third requirement of the roller module is the ability to mechanically couple to other roller modules in the structure in order to fully define the robot's geometry for both 2D and 3D architectures. The roller modules connect to each other at nodes using three-degree-of-freedom universal joints that are comprised of a clevis joint that couples two rods, each free to spin about its axis (Fig. 1D). The length of these rods is determined by the size of the roller modules and the necessary minimum angle between these rods.

The mechanical design of the roller modules and the connections between them must fully constrain the truss structure. Fully constrained means that any external load induces a restoring force that seeks to return the structure back to an equilibrium configuration. Our kinematic analysis (Materials and Methods) indicates that the structure is fully constrained if the connection point between a roller module and its neighbor lies along the line that bisects the two segments of tube joined by that roller. To achieve this constraint, we include two guide rings as shown in Fig. S6. Each guide ring is attached to the body of the roller module through arms that rotate about a pin joint concentric with the top roller of in a pair of rollers. In addition, we place gear teeth on the arms supporting the guide rings to couple the motion of the guide rings. We call these arms geared angle constraints (Fig. S6). Together, the guide rings and the geared angle constraints ensure that a central axis of the roller module bisects the two segments of tube, which in turn ensures that the truss structure is fully constrained.

Tradeoffs: Workspace, Efficiency, and Speed

In this section, we discuss the tradeoffs inherent in the isoperimetric robot design and compare this robot to truss and pneumatically actuated robots. In the first set of comparisons, we examine the effect of kinematic differences between an isoperimetric robot and a conventional truss robot on their respective workspace. Next, we analyze how these kinematic differences affect efficiency and speed of movements. In the last set of comparisons, we examine the effect of the power source—electric motors for the isoperimetric robots and microcompressors for pneumatically actuated robots—on efficiency and speed.

Effects of Kinematic Differences on Workspace

In this section, we qualitatively then quantitatively compare the workspace of a conventional truss robot with that of our robot. Qualitatively, in the conventional truss robot, each edge is a linear actuator with a fixed amount of material that is locally reconfigured to change the edge length. In our robot, each edge can exchange material with other edges in order to change length. This reallocation of material is conceptually similar to changing the shape of a fixed mass of clay: while the shape can change dramatically, the total amount of material must remain the same. In many cases, our concept allows for larger extremes in the length of an individual edge than does a conventional truss robot. However, it also necessitates coupling for changes in the length of edges that are part of the same tube. Each individual tube in the architecture represents another constraint on the achievable configuration space and a potential reduction of the workspace. As a result, an isoperimetric robot will have fewer degrees of freedom than a robot composed of linear actuators with the same graphical structure. Therefore, some motions that are possible for a conventional truss robot are impossible for our robots. The octahedron robot, for example, cannot reduce its total edge length to become a smaller regular octahedron, even though its enclosed volume can substantially change. The mathematical form of these constraints is discussed in the kinematics section (Materials and Methods).

Next, we quantitatively compare the reachable workspaces of the top node of three different 2D triangular robot architectures: an isoperimetric robot with two active roller modules, a conventional truss robot with a linear actuator on each edge, and a conventional truss robot with linear actuators on two edges and supported by two pinned nodes (Fig. 8 and Movie S12). The workspace of our robot completely covers the workspace of the robot composed of three linear actuators, which in turn completely covers the workspace of the robot composed of two linear actuators. The workspace of our robot is 3.4 times larger than the workspace of the robot composed of three linear actuators and 6.8 times larger than the workspace of the robot composed of two linear actuators. These results indicate that in some cases, the isoperimetric architecture may increase a robot's workspace.

Effects of Kinematic Differences on Efficiency and Speed

In this section, we first next qualitatively, then quantitatively, compare how the kinematics of an isoperimetric robot and a truss robot affect the efficiency and speed of motion. Qualitatively, the added constraints on the isoperimetric robot mean certain motions require much more energy or must be performed more slowly than others—a factor that should be considered when planning movements. This can be explained as follows. Unlike in a truss robot, the number of actuators (for our robot, roller modules) needed to change the robot's configuration is not necessarily equal to the number of edges that are changing in length. For example, exchanging length between the two edges adjacent to the same active roller module (Edges 1 and 2 in Fig. 8A) requires only the energy to operate one roller module. However, exchanging length between edges separated by multiple active roller modules (Edge 1 and 3) requires multiple roller modules to drive. These effects are exacerbated if a single tube covers more than 3 edges in a triangle, as illustrated in Fig. 2D and 2E. The coupling between edge length changes and the routing of the tube also affects the rate of change of different edge lengths. For the robot in Fig. 8A, Edge 2 can lengthen at twice the maximum speed of the rollers and hence twice the maximum speed of Edges 1 and 3 due to the fact that it has active rollers on both ends. However, it can only extend at maximum speed if both Edges 1 and 3 are contracting at the maximum speed. These dependencies illustrate that the energy required to perform a given motion and the speed at which edge lengths can change depend on the architecture of the graph, not just the parameters of the actuators as in a truss robot composed of linear actuators.

We quantify these differences by comparing the motions of the robots in Fig. 8. Fig. 8D shows the manipulability index, μ (*50*), for Node 2 throughout the two robots' respective workspaces. The manipulability index is the volume of the manipulability ellipsoid which represents the node velocity resulting from normalized actuator inputs. Larger manipulability indices correspond to larger end effector motions given fixed actuator inputs. The manipulability index is higher for the isoperimetric robot than the robot with two linear actuators across the shared workspace, indicating the possibility of faster motions, but with the corresponding result that higher actuator torques are required to resist external loads. For the robot with three linear actuators, the robot has redundancy to the task of positioning Node 2, which we exploit to maximize the manipulability. Even so, the isoperimetric robot has higher manipulability in a portion of the shared workspace. To further examine this effect, we examine the energy required to move Node 2 of robots with two degrees of freedom (A and C) between a set of randomly generated waypoints while the robot is subject to gravitational and inertial loads (details in S8). The energy output is slightly lower for the isoperimetric robot for low frequency motions. However, as the frequency of motion increases, the required output energy increases faster for the isoperimetric robot than for the truss robot (Fig. 8E). For a prescribed motion of Node 2, Node 3 of the isoperimetric robot must also move to maintain the constant perimeter. The additional motion of Node 3 is increasingly costly as frequency increases and dynamic effects become more pronounced. Furthermore, the individual contributions to output energy from the linear actuators are nearly identical. Meanwhile, one of the roller modules in the isoperimetric robot exerts much more energy than the other. These results indicate that the coupled nature of motion in isoperimetric robots creates tradeoffs in both speed and efficiency.

Effect of Power Source on Efficiency and Speed

Finally, we compare efficiency and speed of different robots based on their use of either electric motors or microcompressors as an energy source. We compare robot A driven by electric motors with two different types of robot C: one of linear actuators driven directly by electric motors and one of pneumatic cylinders driven by microcompressors (details in S8). In this comparison, we use commercially available components to investigate the qualitative characteristics of these devices. We cannot assume the quantitative results will apply to all commercially available components or reveal fundamental limitations of these technologies. We find that robot A is less efficient than the motorized robot C (Fig. 8F), despite the energy output advantages seen in Fig. 8E. This is due to the uneven distribution of load among the two actuators. We find that the minimum time in which the microcompressor-driven robot C can move between waypoints is much slower than the motor-driven robots, yet it is potentially more efficient at low speeds. However, we observe that the time to execute trajectories for the microcompressor-driven robot C depends heavily on the diameter of the pneumatic cylinder considered. Increasing the size of a robot driven by a microcompressor increases the area the compressed gas exerts a pressure on, effectively increasing the gear ratio: this increases the force output and reduces the speed. This effect is observed in the untethered soft robot presented in (6). The authors built their robot at a relatively large scale (length of 0.65 m) in order to accommodate commercially available compressors. The increase in size to accommodate commercial components had the effect of reducing speed (reported speeds of approximately 18 m/hr or 28 body lengths per hour). Our robot is larger, but, as it does not experience the same effect of gear ratio change, it achieves faster locomotion speeds (216 m/hr, or 128 body lengths per hour).

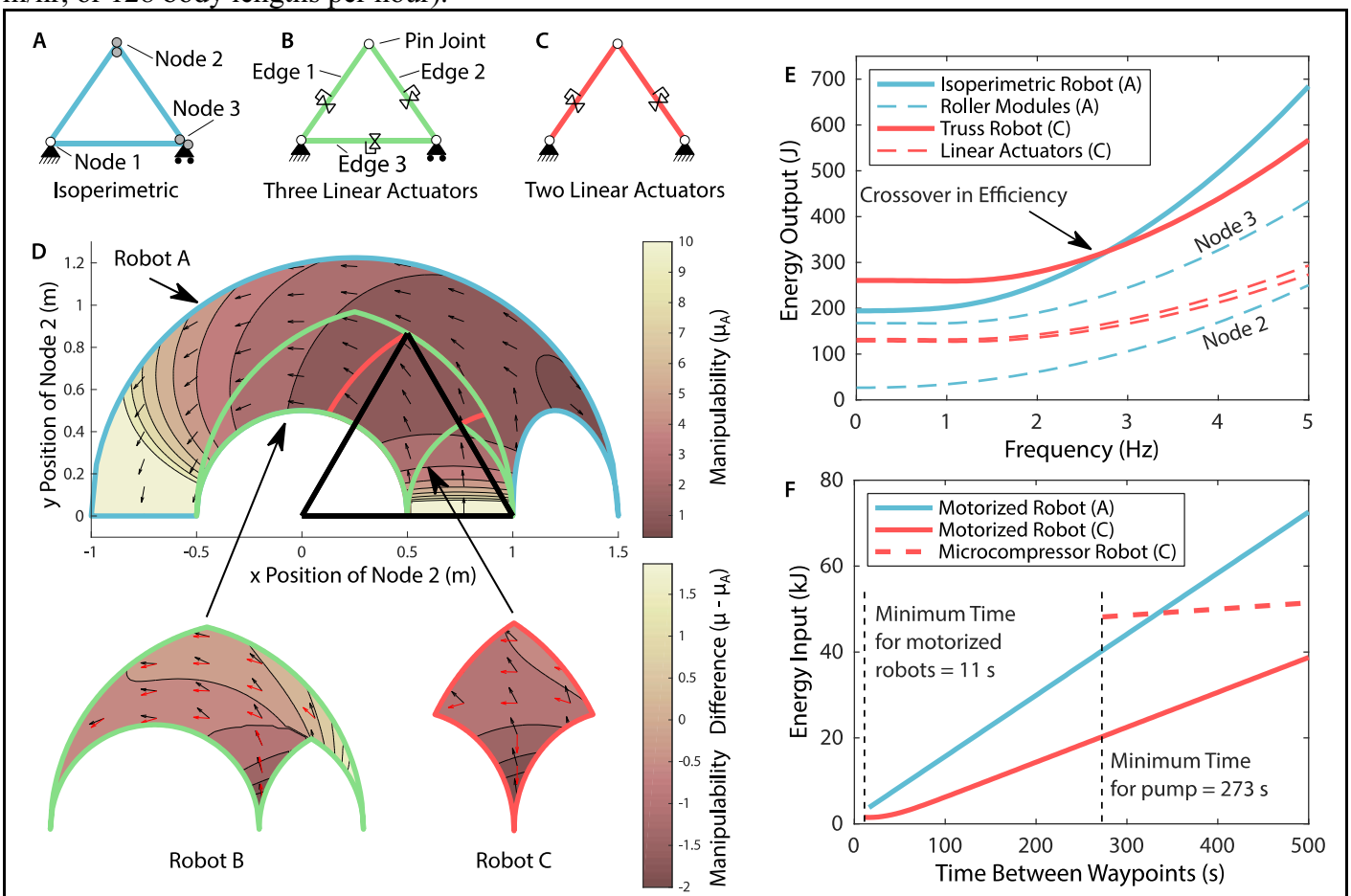

Fig. 8. Comparison of three different robots: **(A)** An isoperimetric robot, **(B)** a truss robot with three linear actuators, and **(C)** a truss robot with two linear actuators. **(D)** The workspaces and manipulability index, μ, of Node 2 for each robot. The minimum edge length for all robots is 0.5 m, and the maximum length of linear actuators in B and C is 1 m. The total edge length of the isoperimetric robot is the maximum perimeter of the truss robots (3 m). The black (red) arrows indicate the direction of maximum velocity for

Node 2 of robot A (robots B and C). (**E**) The effect of frequency on the energy required to move Node 2 between 50 waypoints within the shared workspace for robots A and C. With increased frequency the isoperimetric robot become less efficient due to the coupled motion of Nodes 2 and 3. (**F**) Required energy to move the end effector between waypoints when driven by a specific electric motor and C when driven by either the same motor or a microcompressor with comparable mass. The systems driven by an electric motor are faster than the systems driven by the microcompressor.

Discussion

Here we discuss the implications of the isoperimetric concept in terms of the softness, scaling, and applications of the resultant robots.

In terms of softness, our robots differ from most devices in the field of soft robotics. While our robots are like most soft robots in that they comprise a mixture of compliant materials (fabric and air) and some rigid components, they differ in that their rigid components are external instead of internal. While at first glance this may seem limiting, it is a similar architecture to that found in insects, where rigid exoskeletal segments are joined by compliant tissue (*51*). In our case, the natural compliance of the beams connecting the rigid nodes creates an effective stiffness that is far below the actual stiffness of node material. Further, the mechanical fuse-type behavior limits the overall maximum load that can be applied at a node. Naturally, the compliant tubes afford some robustness to the roller modules because the tubes can conform to misalignment of the rollers and prevent large forces and impacts from being transmitted between roller modules. Additionally, it may be possible in future work to replace the roller modules with soft bodied analogues to further increase the safety and robustness of the system.

In this work, we presented versions of our robot at an approximately human scale. A key question for understanding the broader applicability of this type of robot is how performance changes with robot size scale. If we scale all dimensions uniformly, then as the length L increases, the mass of the robot increases roughly with L^3. The strength of the structure is governed by the mechanics of inflated beams and is a function of the geometry, material properties, and internal pressure which precludes extracting a simple scaling law. However, if we assume that the strength of the structure can be approximated by considering the inflated tubes as Euler beams that fail due to buckling, the load bearing capacity increases with L^2, a slower rate of increase than the robot's mass, meaning that isometric upscaling will eventually result in robots that cannot support their weight. However, given that buckling strength depends on the fourth power of tube diameter, slightly positive allometric scaling of tube diameter would enable increased robot sizes.

We envision a variety of potential applications for robots based on our concept. For example, in planetary rover missions, a robot using our architecture could deflate and pack in a small volume for launch, inflate upon landing, and then perform missions untethered from any energy source. The soft nature of the robot would enable robustness, and the robot could change its shape to navigate challenging terrain or perform tasks that may not be known *a priori*. The compliance and shape change of the robot could make it suitable for several tasks involving humans. For example, the robot could work alongside workers, holding parts in place as the worker bolts them in place. In the classroom, the modularity and soft nature of the robotic system make it a potentially valuable educational tool. Students could create many different robots with a single collection of hardware, and then physically interact with the robot. By including a much larger number of roller modules in a robot, the robot could function as a shape display, dynamically changing shape as a sort of high-refresh-rate 3D printer (*52*). Incorporating touch-sensitive fabric into the structure could allow users to directly interact with the displayed shapes. More broadly, the modularity allows the same hardware to build a diverse family of robots—the same roller modules can be used with new tube routings to create

new robots. If the user needed a robot to reach through a long, narrow passageway, they could assemble a chain-like robot; then for a locomoting robot, they could reassemble into a spherical shape.

Our robotic concept is built upon a synthesis of concepts from collective, truss-like, and soft robots. We demonstrated its collective nature by creating—from identical, one-degree-of-freedom subunits—two 2D architectures and one 3D architecture. We showed the robots' truss-like behavior through dramatic shape change, load carrying, and locomotion. We demonstrated and characterized their compliant nature through a mechanical fuse behavior and an ability to engulf, grasp, and manipulate objects. Beyond these demonstrations, we presented analysis for the design of robot subcomponents. We developed and validated a model that predicts the stiffness of a joint formed by a roller modular, and experimentally studied the effect of geometric parameters on the force required to drive a roller along the tube. Finally, we examined tradeoffs, comparing the workspace, efficiency, and speed of a robot based on our concept to these characteristics of similar robots. Our work introduces the isoperimetric concept to the field of soft robotics for the structure and movement of untethered pneumatic robots.

Materials and Methods

Construction

The inflatable tubes we use in our demonstration are constructed out of an outer layer of heavy fabric and an inner air-tight bladder. We selected a commercially available fabric with minimal stretch along the 45-degree bias. This fabric is a 200-denier nylon fabric with an oxford weave and a urethane coating (Seattle Fabrics Inc.). The fabric is cut into a long rectangular piece and sewn together with a plain seam and a straight stitch. A small hole is punched into the fabric for a pressure line connector. The inner bladder is formed from a low-density polyethylene tube (Hudson Exchange). This tube is cut to length, a hole is punched in its side for the fitting, and the ends are heat sealed. The inner bladder is inserted into the fabric outer layer and the ends of the outer layer are sewn shut with a straight stitch. Finally, a threaded through-wall pipe fitting is fastened in place where the holes in each layer align. In practice we inflated the tubes to approximately 40 kPa.

The housing of the roller module is created with laser cut polyoxymethylene (POM) sheets. These pieces are fastened together with standoffs and corner brackets. The housing contains holes to lightly press fit ball bearings that support the rotation of the rollers and the gear train. The rollers are steel D-shafts wrapped in a non-slip material (Dycem). External grooves are cut into the rollers where retaining rings are placed to locate the rollers with respect to the ball bearings. The custom gear train has a speed multiplier of 3 which was selected for geometric convenience. Our gear train is driven by a direct current motor with a planetary, reducing gear box with a gear ratio of about 139:1 (ServoCity #638320). The motor is driven by a Cytron MD10C motor driver in a drive-brake control method. The motor driver is commanded by a Teensy 3.2 microcontroller which uses an nRF24l01+ radio transceiver to receive position commands from an offboard laptop. The laptop is not a necessary component as the position commands could be stored on the microcontroller. The laptop provides a convenient user interface to send commands to the microcontrollers. When multiple roller modules are connected at a vertex, a single microcontroller controls all the connected roller modules. When possible, we connect passive modules together to reduce the number of microcontrollers. Power was delivered to each roller module by a 1300 mAh, 75 C, 14.8 V lithium polymer battery manufactured by Tattu. The mass of each roller module is 2.83 kg, and each passive module weighs 1.6 kg. The complete octahedron robot (8 active roller modules, 4 passive modules, and the fabric tubes) weighs approximately 29 kg. The 2D robots weigh 22 kg (three tubes) and 19 kg (single tube). A part callout for the roller module is shown in Fig. S6.

Control

Each roller module is responsible for controlling its position in 1D along the inflated tube. The microcontroller tracks the position of the connected roller modules along their tubes using the motor encoders and utilizes a PID controller to drive the rollers to the target position. To determine the desired commands to broadcast to the robot, we experiment with different commands using a computer simulation that propagates the kinematics presented in Materials and Methods.

Kinematics

Understanding the kinematics of the system allows us to analyze and control the robot's motion, understand the forces the actuators must apply during operation, and informs what types of physical constraints we must include in the mechanical design of the roller module. We first present the kinematics relating the motion of the roller modules to the position of the nodes in the idealized case where the center axis of each edge intersects exactly at the joints of the structure. We then expand this treatment to discuss the kinematics of the structure when the effective centers of rotation do not coincide with the joints, as is a physical necessity of the robot. The kinematics of a network of linear actuators connected into an arbitrary structure are presented in (*53*). We summarize the key results from that work here and extend the kinematics to the case of a robot where several edges are composed of a single tube.

Idealized Kinematics

We model the robot as a framework, a mathematical structure that consists of a graph G and vertex positions $p_i \in \mathbb{R}^d$. The graph is denoted as $G = \{V, E\}$, where $V = \{1, \dots, n\}$ are the vertices of the graph, and $E = \{\{i,j\}_1, \{i,j\}_2 \dots \{i,j\}_{N_L}\}$ are the undirected edges of the graph. The geometry of the robot (assuming no deflection of the members) is fully represented by the concatenation of all vertex positions $x = [p_1^{\mathrm{T}}, p_2^T, p_3^T, \dots p_N^{\mathrm{T}}]^T$. The length of each edge can be obtained

$$L_{\mathrm{k}} = \left\| p_i - p_j \right\| \forall \{i,j\}_k \in E. \tag{1}$$

We form the differential kinematics that relate the changes in the edge lengths to the changes in the node positions as follows:

$$\frac{dL_k^2}{dt} = 2\, L_k\, \dot{L}_k = \ 2\big(p_i - p_j\big)^T\, \dot{p}_i \ + \ 2\big(p_j - p_i\big)^T\, \dot{p}_j\,. \tag{2}$$

Rearranging this into matrix form, we obtain

$$\dot{L} = R(x)\dot{x}. \tag{3}$$

We also express the constraints that ground the robot to the outside world in the form

$$C\dot{x} = 0, \tag{4}$$

where C is a matrix that constrains the structure to the outside world. In practice we identify three ground nodes of the robot and pick C such that one ground node is fixed in all directions, the second is fixed in two directions, and the third is fixed only in the direction normal to the ground. Combining (3) and (4) we obtain:

$$\begin{bmatrix} \dot{L} \\ 0 \end{bmatrix} = \begin{bmatrix} R(x) \\ C \end{bmatrix} \dot{x}. \tag{5}$$

If $[R(x)^T C^T]^T$ is invertible, we find the forward kinematics (Jacobian) that relates the rate of change of the actuator edges to the motion of the nodes

$$\dot{x} = \begin{bmatrix} R(x) \\ C \end{bmatrix}^{-1} \begin{bmatrix} I_{N_L} \\ 0 \end{bmatrix} \dot{L} = J_L(x)\dot{L}. \tag{6}$$

The matrix $[R(x)^T C^T]^T$ is invertible when the robot is minimally infinitesimally rigid, which intuitively means that the robot has the minimum number of edges to ensure static independence, and that each edge is capable of changing length independently. For the matrix to be square and invertible, the number of edges in the network must be $3n - 6$ for the 3D robot, and $2n - 3$ for the 2D robot. Using the well-known relationship between the Jacobian and externally applied forces, we write

$$J(x)^T F = \tau_L, \tag{7}$$

where τ_L is the vector of forces on the linear actuators and F is a vector of forces applied at the nodes.

We now incorporate the constraint that several of the linear members in the robot are composed of a single tube, and that their total length must remain constant. In our treatment we will assume that the path defined by the tubes each form a cycle, meaning that they begin and end at the same node. This allows us the mechanical convenience of connecting the beginning and end of the tube at a passive module. Including paths that start and end at different nodes requires only minor modification. The path of the tube or tubes through the robot is defined by an ordered pair of nodes where each stop at a node corresponds with a roller module, which we number 1 to N_{roller}. We represent these paths as a matrix $B_{all}(\mathrm{G}) \in \mathbb{R}^{N_{roller}, N_L}$. Each column of B_{all} corresponds to one edge of the graph and has exactly two nonzero entries: a 1 in the row corresponding to the tail node of the directed edge and a -1 at the row corresponding to the head of the directed edge. This matrix allows us to relate the velocity of the rollers to the rate of change of the edge lengths:

$$\dot{L} = {B_{all}}^T \dot{\theta}. \tag{8}$$

where θ corresponds to the position of each of the rollers along the tube. To relate the motion of the rollers directly to the motion of the nodes, we combine (6) and (8) to obtain:

$$\begin{bmatrix} R(x) \\ C \end{bmatrix}^{-1} \begin{bmatrix} {B_{all}}^T \\ 0 \end{bmatrix} \dot{\theta} = \dot{x} = J_\theta(x)\dot{\theta}. \tag{9}$$

The Jacobian $J_\theta(x)$ relates the motor motions to node motions, which also allows us to quantify the torque required from the motors to hold a particular configuration as $\tau_{roller} = J_\theta(x)^T F$.

We note that the sum of all of the edge lengths of the structure is obtained as $1^T L$. We can confirm the total length of the shared member is unchanged for any combination of roller velocity inputs by showing that $1^T B^T = 0$, which is a result of the construction of the B matrix, as we have ensured that each column sums to 0.

If each tube in the robot is a single continuous loop with no end, all the roller modules could run at the same speed and the tube would move continuously while all the nodes remain stationary, as indicated by the fact that $B^T 1 = 0$. In practice, we do not include a motor at the node that makes up the first and last connection for each tube, which corresponds to removing the elements of $\dot{\theta}$ and columns of B that correspond to the first and last node of each tube in the robot.

Kinematics in the Presence of Offsets

In practice, it is not possible for the edges to intersect at the nodes due to the large size of the tubes as well as the double-roller design of each roller module (Fig. 6C). In the presence of these offsets, we represent the kinematic state of each roller module as the position of three points. These points are illustrated in Fig. S7 and are the point where two roller modules connect (denoted point A) and the point at the center of each pair of rollers in plane with the inflated tube (points B and D). We denote the point at the opposite end of each tube segment from points B and D as points C and E, respectively. We want to impose sufficient constraints in the physical design of the roller module so fully constrain the kinematic state of all roller modules (points A, B, and D for each module). For a robot in 3D, each new point introduced into the kinematic state introduces 3 new degrees of freedom. For each roller module, we must remove 6 degrees of freedom. We have chosen to include two guide rings that are geared together such that they, along with the mechanical construction of the roller module, enable the following mathematical constraints:

- All edges in the triangle formed by points A, B and D are constant length. The resulting forces are provided by the physical structure of the roller module. This imposes three constraints which are of the same form as the constraints in (1). We take the derivative of these constraints and rearrange them into the matrix $R_{\mathrm{node}}(x)$.
- A constraint that the angle CBD is equal to the angle EDB. This constraint is provided by gear teeth that are included onto the arms of the angle constraint show in Fig. S7. This imposes one constraint, which is expressed:

$$\frac{(x_d - x_b)^T(x_c - x_b)}{\|(x_d - x_b)\|\|(x_c - x_b)\|} = \frac{(x_e - x_c)^T(x_b - x_c)}{\|(x_e - x_c)\|\|(x_b - x_c)\|}. \tag{10}$$

We take the derivative of this constraint for each roller module in the network and put the result into a matrix $R_{bisect}(x)$.

- A constraint that Point A remains in the plane defined by the points B, C, and D and the plane defined by the points B, C, and E. This constraint requires coupling between the edges and the rollers in a direction normal to both edges. This imposes two constraints, which are enforced by the guide rings. This constraint is only necessary when the robot is in 3D. This constraint is expressed:

$$\frac{(x_a - x_b)^T\big((x_c - x_b) \times (x_d - x_b)\big)}{\|x_d - x_b\|\|(x_c - x_b) \times (x_d - x_b)\|} = 0, \tag{11}$$

and

$$\frac{(x_a - x_c)^T\big((x_b - x_c) \times (x_e - x_c)\big)}{\|x_e - x_c\|\|(x_b - x_c) \times (x_e - x_c)\|} = 0. \tag{12}$$

We again take the derivative of each of these constraints in the current configuration and put the result into the matrix $R_{planar}(x)$

We combine these results to form the following result:

$$\begin{bmatrix} R_{tube}(x) \\ R_{node}(x) \\ R_{bisect}(x) \\ R_{planar}(x) \\ C \end{bmatrix} \dot{x} = \begin{bmatrix} \dot{L}_{tube} \\ 0 \end{bmatrix}. \tag{13}$$

By including the constraints we have specified, we ensure that this combined matrix is square. If this matrix is of full rank, (which is a function of the current node positions) then the overall structure is infinitesimally minimally rigid, and the structure cannot move relative to itself without violating the constraints. If the matrix is invertible,

$$\dot{x} = \begin{bmatrix} R_{tube}(x) \\ R_{node}(x) \\ R_{bisect}(x) \\ R_{planar}(x)C \end{bmatrix}^{-1} \begin{bmatrix} B^T \\ 0 \end{bmatrix} \dot{\theta} = J_{\theta,full}(x)\dot{\theta}. \tag{14}$$

We can also extract the axial loads on the different members through $\tau_L = J^T_{\theta,full}(x)F$. We note that these are the resulting forces assuming that the edges are rigid. In practice, the compliance in the inflated tubes may alter the actual configuration and loads. However, this method generates a reasonable estimate of the loading conditions on the inflated tubes and the torques that must be exerted by the motors.

References and Notes

1. M. Yim, W. M. Shen, B Salemi, D. Rus, M. Moll, H. Lipson, E. Klavins, G. S. Chirikjian, Modular self-reconfigurable robot systems [grand challenges of robotics], *IEEE Robotics & Automation Magazine*, **14**, 43-52, (2007).
2. H. Ahmadzadeh, E. Masehian, M. Asadpour, Modular robotic systems: characteristics and applications. *Journal of Intelligent & Robotic Systems*. 81, 317-357 (2016).
3. J. W. Romanishin, K. Gilpin, D. Rus, M-blocks: Momentum-driven, magnetic modular robots, in *Proceedings of the 2013 IEEE/RSJ International Conference on Intelligent Robots and Systems*, 3 November 2013, pp. 4288-4295.
4. G. Jing, T. Tosun, M. Yim, H. Kress-Gazit, An End-To-End System for Accomplishing Tasks with Modular Robots, in *Proceedings of Robotics: Science and Systems* June 2016.
5. F. Nigl, S. Li, J. E. Blum, H. Lipson, Structure-reconfiguring robots: Autonomous truss reconfiguration and manipulation, *IEEE Robotics & Automation Magazine*, **20,** 60-71, (2013).
6. S. K. Yun, D. A. Hjelle, E. Schweikardt, H. Lipson, D. Rus, Planning the reconfiguration of grounded truss structures with truss climbing robots that carry truss elements, in *Proceedings of the 2009 IEEE International Conference on Robotics and Automation* 12 May 2009, pp. 1327-1333.
7. B. Jenett, A. Abdel-Rahman, K Cheung, N Gershenfeld, Material–Robot System for Assembly of Discrete Cellular Structures. *IEEE Robotics and Automation Letters*. **4**, 4019-26 (2019).
8. K. H. Petersen, R. Nagpal, J.K. Werfel, Termes: An autonomous robotic system for three-dimensional collective construction. *Robotics: science and systems*. **7**. 2011.
9. G. J. Hamlin, A. C. Sanderson, Tetrobot: A modular approach to parallel robotics. *IEEE Robotics & Automation Magazine*. March 4 1997, 4(1): 42-50.
10. R. Kovacs, A. Ion, P. Lopes, T. Oesterreich, J. Filter, P. Otto, T. Arndt, N. Ring, M. Witte, A. Synytsia, P. Baudisch, TrussFormer: 3D Printing Large Kinetic Structures. In *Proceedings of the 31st Annual ACM Symposium on User Interface Software and Technology*, 11 October 2018, pp. 113-125.
11. P. C. Hughes, W. G. Sincarsin, K. A. Carroll, Trussarm—a variable-geometry-truss manipulator. *Journal of Intelligent Material Systems and Structures*, **2**, 148-160 (1991).
12. S. Curtis, M. Brandt, G. Bowers, G. Brown, C. Cheung, C. Cooperider, M. Desch, N. Desch, J. Dorband, K. Gregory, K. Lee, Tetrahedral robotics for space exploration. In Proceedings of 2007 IEEE Aerospace Conference, 3 March 2007 pp. 1-9.
13. J. C. Zagal, C. Armstrong, S. Li, Deformable octahedron burrowing robot, in *Proceedings of Artificial Life Conference (International Society of Artificial Life, 2012)*. 12 July 2012. pp. 431-438.
14. A. Spinos, D. Carroll, T. Kientz, M. Yim, Variable topology truss: Design and analysis, in *Proceedings of the 2017 IEEE/RSJ International Conference on Intelligent Robots and Systems,* 24 September 2017, pp. 2717-2722.
15. J. Friesen, A. Pogue, T. Bewley, M. de Oliveira, R. Skelton, V. Sunspiral, DuCTT: A tensegrity robot for exploring duct systems, in *Proceedings of the 2014 IEEE International Conference on Robotics and Automation* 31 May 2014, pp. 4222-4228.
16. A. Spinos, M. Yim, Towards a variable topology truss for shoring, in *Proceedings of the 2017 14th International Conference on Ubiquitous Robots and Ambient Intelligence*, Jun 28 2017 pp. 244-249.
17. A. Lyder, R. F. Garcia, K. Stoy, Mechanical design of odin, an extendable heterogeneous deformable modular robot, in *Proceedings of 2008 IEEE/RSJ International Conference on Intelligent Robots and Systems* Sep 22 2008 pp. 883-888.
18. C. H. Yu, K. Haller, D. Ingber, R. Nagpal, Morpho: A self-deformable modular robot inspired by cellular structure, in *Proceedings of the 2008 IEEE/RSJ International Conference on Intelligent Robots and Systems,* 22 September 2008, pp. 3571-3578.

19. S. Takei, M. Iida, T, Naemura, Kinereels: extension actuators for dynamic 3d shape, in *ACM SIGGRAPH 2011 Posters* 7 Aug 2011 (p. 84).
20. S. Jeong, B. Kim, S. Park, E. Park, A. Spinos, D. Carroll, T. Tsabedze, Y. Weng, T. Seo, M. Yim, F.C. Park, Variable Topology Truss: Hardware Overview, Reconfiguration Planning and Locomotion, in *Proceedings of the 2018 15th International Conference on Ubiquitous Robots,* Jun 26 2018 pp. 610-615.
21. Z. M. Hammond, N. S. Usevitch, E. W. Hawkes, S. Follmer, Pneumatic reel actuator: Design, modeling, and implementation, in *Proceedings of 2017 IEEE International Conference on Robotics and Automation*, 29 May 2017, pp. 626-633.
22. N. S. Usevitch, A. M. Okamura, E. W. Hawkes, APAM: antagonistic pneumatic artificial muscle, in *Proceedings of the 2018 IEEE International Conference on Robotics and Automation,* 21 May 2018, pp. 1539-1546.
23. A. P. Sabelhaus, J. Bruce, K. Caluwaerts, P. Manovi, R. F. Firoozi, S. Dobi, A. M. Agogino, V. SunSpiral, System design and locomotion of SUPERball, an untethered tensegrity robot, in *Proceedings of the 2015 IEEE international conference on robotics and automation,* 26 May 2015 pp. 2867-2873.
24. L.H. Chen, K Kim, E Tang, K Li, R House, El Zhu, K Fountain, A.M. Agogino, A. Agogino, V. Sunspiral, E. Jung. Soft spherical tensegrity robot design using rod-centered actuation and control. *Journal of Mechanisms and Robotics*. **2**, 2017
25. Bruce J, Sabelhaus AP, Chen Y, Lu D, Morse K, Milam S, Caluwaerts K, Agogino AM, SunSpiral V. SUPERball: Exploring tensegrities for planetary probes, in *Proceedings of 12th International Symposium on Artificial Intelligence, Robotics and Automation in Space (i-SAIRAS 2014)*, Montreal, Canada, 17 to 19 June 2014.
26. C. Paul, J. W. Roberts, H. Lipson, F. V. Cuevas, Gait production in a tensegrity based robot, in *Proceedings of 2005 IEEE International Conference on Advanced Robotics.* 18 July 2005, pp. 216-222.
27. S. Murata, D. Jodoi, H. Furuya, Y. Terada, K. Takadama. Inflatable tensegrity module for a large-scale space structure and its construction scenario, in the 56th International Astronautical Congress (2005).
28. J. Dessi-Olive, J. Case, M. Koliner, V.T. Meda, Self-deploying tensegrity structures with inflatable struts, in *Proceedings of the International Association for Shell and Spatial Structures* (2019).
29. D. Rus and M. T. Tolley, Design, Fabrication and Control of Soft Robots. *Nature*. **521**, 467-475 (2015).
30. C. Majidi. Soft robotics: a perspective—current trends and prospects for the future. *Soft Robotics*. **1**, 5-11. (2014)
31. E. W. Hawkes, M. R. Cutkosky, Design of materials and mechanisms for responsive robots. *Annual Review of Control, Robotics, and Autonomous Systems.* **1**, 359-384 (2018).
32. S. I. Rich, R. J. Wood, C. Majidi, Untethered soft robotics, *Nature Electronics.* **2** 102 (2018).
33. X. Huang, K. Kumar, M. K. Jawed, A. M. Nasab, Z. Ye, W. Shan, C. Majidi, Chasing biomimetic locomotion speeds: Creating untethered soft robots with shape memory alloy actuators. *Sci. Robotics* **3,** 25 (2018).
34. M. T. Tolley R. F. Shepherd, B. Mosadegh, K. C. Galloway, M. Wehner, M. Karpelson, R. J. Wood, G. M. Whitesides, A Resilient, Untethered Soft Robot. *Soft Robotics.* **1**, 213-223 (2014).
35. R. Niiyama, D. Rus, S. Kim, Pouch motors: Printable/inflatable soft actuators for robotics, in *Proceedings of the 2014 IEEE International Conference on Robotics and Automation.* 31 May 2014, pp. 6332-6337.
36. A. D. Marchese, C. D. Onal, D. Rus, Autonomous soft robotic fish capable of escape maneuvers using fluidic elastomer actuators. *Soft Robotics.* **1(1)**, 75-87 (2014).

37. M. Wehner, R. L. Truby, D. J. Fitzgerald, B. Mosadegh, G. M. Whitesides, J. A. Lewis, and R. J. Wood, An Integrated Design and Fabrication Strategy for Entirely Soft, Autonomous Robots. *Nature* **536**, 451–455 (2016).
38. N. W. Bartlett, M. T. Tolley, J. T. Overvelde, J. C. Weaver, B. Mosadegh, K. Bertoldi, G. M. Whitesides, and R. J. Wood, A 3D-printed, functionally graded soft robot powered by combustion. *Science* **349**, 161-165 (2015).
39. M. Loepfe, C. M. Schumacher, U. B. Lustenberger, and W. J. Stark, An untethered, jumping roly-poly soft robot driven by combustion. *Soft Robotics* **2,** 33-41 (2015).
40. M. Wehner, M. T. Tolley, Y. Mengüç, Y. L. Park, A. Mozeika,Y. Ding, C. Onal, R. F. Shepherd, G. M. Whitesides, R. J. Wood. Pneumatic energy sources for autonomous and wearable soft robotics, *Soft robotics*. 2014 Dec 1;1(4):263-74.
41. M. Takeichi, K. Suzumori, G. Endo, H. Nabae, Development of a 20-m-long Giacometti arm with balloon body based on kinematic model with air resistance, in *Proceedings of the 2017 IEEE/RSJ International Conference on Intelligent Robots and Systems*, 24 September 2017, pp. 2710-2716.
42. S. Voisembert, A. Riwan, N. Mechbal, A. Barraco, A novel inflatable robot with constant and continuous volume, in *Proceedings of the 2011 IEEE International Conference on Robotics and Automation* 9 May 2011, pp. 5843-5848.
43. Y. A. Seong, R. Niiyama, Y. Kawahara, Low-pressure Soft Inflatable Joint Driven by inner Tendon. *2019 2nd IEEE International Conference on Soft Robotics,* 14 April 2019, pp. 37-42.
44. A. Stilli, H. A. Wurdemann, K. Althoefer, A novel concept for safe, stiffness-controllable robot links. *Soft Robotics*. **4** 16-22 (2017).
45. H. Sareen, U. Umapathi, P. Shin, Y. Kakehi, J. Ou, H. Ishii, P. Maes, Printflatables: printing human-scale, functional and dynamic inflatable objects, in *Proceedings of the 2017 CHI Conference on Human Factors in Computing Systems,* May 2 2017. pp. 3669-3680.
46. S. Swaminathan, M. Rivera, R. Kang, Z. Luo, K. B. Ozutemiz, S. E. Hudson, Input, Output and Construction Methods for Custom Fabrication of Room-Scale Deployable Pneumatic Structures, in *Proceedings of the ACM on Interactive, Mobile, Wearable and Ubiquitous Technologies.* **3**, 2019.
47. W. B. Fichter, A theory for inflated thin-wall cylindrical beams, National Aeronautics and Space Administration, NASA TN D-3466,1966.
48. R. L. Comer and S. Levy, Deflections of an inflated circular-cylindrical cantilever beam, *AIAA Journal*, **1**,1652–1655, 1963.
49. Y. He, W. Chen, Experiment and theoretical analysis study of etfe inflatable tubes, *International Journal of Aerospace Engineering,* 2014.
50. T. Yoshikawa, Manipulability of robotic mechanisms, *International Journal of Robotics Research*, **4**, 3-9, 1985.
51. S. A. Wainwright, W. D. Biggs, J. D. Currey, *Mechanical design in organisms* (Princeton University Press, 1982).
52. S. Follmer, D. Leithinger, A. Owal, A. Hogge, H. Ishii, inFORM: dynamic physical affordances and constraints through shape and object actuation, in *User Interface Software and Technology*, 8 October 2013, Vol. 13, pp. 417-426.
53. N. S. Usevitch, Z. Hammond, S. Follmer, M. Schwager, Linear actuator robots: Differential kinematics, controllability, and algorithms for locomotion and shape morphing, in *Proceedings of the 2017 IEEE/RSJ International Conference on Intelligent Robots and Systems,* 24 September 2017, pp. 5361-5367.
54. C. R. Nesler, T. A. Swift, E. J. Rouse, Initial design and experimental evaluation of a pneumatic interference actuator. *Soft robotics*. **5,** 138-148 (2018).
55. J. P. Fay, C. R. Steele, Bending and symmetric pinching of pressurized tubes, *International journal of solids and structures,* **37**, 6917-6931 (2000).

56. K. Wakana, H. Namari, M. Konyo, S. Tadokoro, Pneumatic flexible hollow shaft actuator with high speed and long stroke motion, in *Proceedings of the 2013 IEEE International Conference on Robotics and Automation,* 6 May 2013, pp. 357-363.
57. B. A. Baydere, S. K. Talas, E. Samur, A novel highly-extensible 2-DOF pneumatic actuator for soft robotic applications, *Sensors and Actuators A: Physical.* **281**, 84-94 (2018).
58. R. L. Foote, The volume swept out by a moving planar region, *Mathematics Magazine,* **79,** 289-97 (2006).
59. F. C. Campbell, *Elements of Metallurgy and Engineering Alloys* (ASM International, 2008), chap. 14, pp. 243 – 246.

Acknowledgments

Funding –SF, AMO, EWH, and ZMH acknowledge support from the National Science Foundation under grant no. 1637446. MS and NSU acknowledge support from DARPA YFA under grant no. D18AP00064. MS, SF, EWH, ZMH, and NSU acknowledge support from the National Science Foundation under grant no. 1925030.

Author Contributions - NSU and ZMH designed and built the robot, performed the testing and wrote the manuscript. AMO and MS provided direction and edited the manuscript. SF and EWH defined the project and edited the manuscript.

Competing interests - The authors declare no competing interests

SUPPLEMENTARY MATERIALS

Text

S1: Experimental Setup for Measuring Battery Life

The continuous battery life of the prototype presented in this paper is shown in Fig. S1A. A triangular robot was oriented vertically and one of its roller modules was driven in a cycle pattern while monitoring the energy delivered it (Fig. S1B – S1D). Using the energy consumed and the time elapsed during each cycle, we compute the estimated battery life of the 14.8 V, 1300 mAh, LiPo batteries we use in our demonstrations. These batteries are assumed to store 69.3 KJ of energy which is calculated with the following equation

$$E_{stored} = (1300\ \text{mAh})(14.8\ \text{V})(3600\ \text{sec/h}) = 69.3\ \text{KJ}$$

We note that one of the chief inefficiencies of our design is the motor used in the robot (ServoCity part #638320) exhibit a peak efficiency of less than 30%. Battery life could be substantially improved by using a more efficient motor, or by reducing friction in the custom gear train.

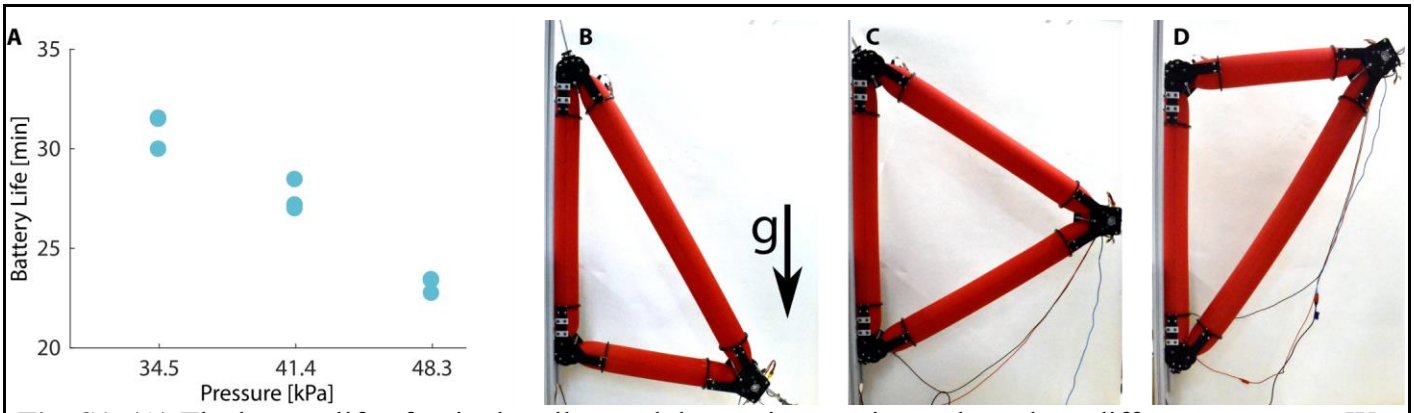

Fig. S1. (**A**) The battery life of a single roller module running continuously at three different pressures. We repeated the test three times per pressure. (**B to D**) The roller module is moved in a cyclic path. The roller module is a part of a triangle oriented vertically so that the roller module moves against gravity. The battery life calculated in (**A**) is extrapolated from the energy drawn and time elapsed during one cycle starting at a low point (**B**) moving upward to a high point (**D**) and then returning to the low point (**B**). The battery used for this calculation is a 14.8 V, 1300 mAh, LiPo battery.

S2: Modeling and Measuring Bending of a Beam Through Rollers

We present a reduced order model to measure the torque required to bend an inflated fabric tube around a set of rollers. Our key assumption is that the tube material is flexible but inextensible, and that the tube will take a shape that maximizes its enclosed volume for a fixed joint angle. These assumptions allow us to write $V = f(\theta)$ and calculate the torque using the principle of virtual work $\tau(\theta) = P\frac{dV(\theta)}{d\theta}$. To use this model requires us to (i) parameterize the shape of the tube, (ii) compute the tube's volume, and (iii) characterize the change in volume with angle. Past work has studied the post-buckling bending response of inflated fabric beams without rollers (*54-55*), as well as models to predict the force exerted on the rollers when the tube is only inflated on one side of the rollers (*56-57*). Our approach will combine elements of these modeling approaches to quantify the change in torque with the angle of a beam passing through a set of rollers.

Shape Parameterization

We parameterize the shape of the tube as shown in Fig. S2A. We assume that the paths along the top and bottom of the inflated membrane are of equal length, smooth (the derivative is continuous everywhere), and that they are composed of a constant curvature section and a straight section when not in contact with the roller. We wish to express the equation of the top and bottom paths as functions of the geometric constant parameters (D, h, R_{roll}, L_{tot}, θ), and two input parameters of our choice that we will later optimize over. We select R_t and R_b as the input parameters and solve for the values for α_t, α_b , c_t and c_b using geometric constraints. First, we relate the tube diameter to four of the geometric parameters:

$$c_b + c_t + R_t + R_b = D.$$

Examining the geometry defining the constant curvature section of tube near the rollers, we can develop two more equations relating known distances:

$$(R_{Roll} + R_t)\cos(\alpha_t + \theta) + c_t = \left(\frac{h}{2} + R_{Roll}\right)\cos(\theta),$$
$$(R_{Roll} + R_b)\cos(\alpha_b + \theta) + c_b = \left(\frac{h}{2} + R_{Roll}\right)\cos(\theta).$$

For the final equation, we express the constraint that the lengths of the top and the bottom paths are equal. This constraint takes the form of a loop closure equation:

$$R_{Roll}\sin(\alpha_t) + R_t\sin(\alpha_t) + R_t\sin(\theta) + \big(L_{tot} - R_{Roll}\alpha_t - R_t(\alpha_t + \theta)\big)\cos(\theta) + D\sin(\theta)$$
$$= R_{Roll}\sin(\alpha_b) + R_b\sin(\alpha_b) - R_b\sin(\theta) + \big(L_{tot} - R_{Roll}\alpha_b - R_b(\alpha_b + \theta)\big)\cos(\theta).$$

We solve these interdependent equations numerically which gives us the shape of the top path of the membrane as $\gamma_{top}(\lambda, \theta, R_t, R_b)$ and the shape of the bottom path of the membrane $\gamma_{bottom}(\lambda, \theta, R_t, R_b)$, where λ is a parameter along the arc length of the tube. For clarity, we denote the collection of the parameters θ, R_t, R_b as p. We assume that the cross section of the tube is described by a square in between two half circles as shown in Fig. S2A. The perimeter of this cross section is held constant at πD, meaning that no wrinkles form in the longitudinal direction along the tube. For a fixed value of λ, $\gamma_{top}(\lambda, p)$ and $\gamma_{bottom}(\lambda, p)$ intersect the cross section respectively at the top and bottom of the cross section on the axis of symmetry. We denote the height of this cross section $h(\lambda, p) = \left|\left|\gamma_{top}(\lambda, p) - \gamma_{bottom}(\lambda, p)\right|\right|$, and the normal vector to the cross section $n(\lambda, p)$. Using the assumption that the perimeter of the cross section is constant, we can write

$$A(\lambda, p) = \pi\frac{h(\lambda,p)}{2}\left(D - \frac{h(\lambda,p)}{2}\right).$$

To compute the volume of the tube we define the center path of the tube as

$$c(\lambda) = \frac{1}{2}\Big(\gamma_{top}(\lambda, p) + \gamma_{bottom}(\lambda, p)\Big)$$

and utilize techniques from (*58*) to write:

$$V(\theta,\ R_t, R_b)\ =\ \int_0^{L_{tot}} A(\lambda, p)\left(\gamma'(\lambda, p) + \big(\gamma(\lambda, p)\ -\ c(\lambda, p)\big)\cdot n'(\lambda, p)\right) d\lambda.$$

We assume that the tube will take the shape that maximizes the volume. We find $V^*(\theta)$ by fixing the value of θ and maximizing the volume with R_t and R_b as free variables:

$$V^*(\theta) = \max_{R_t, R_b} V(\theta, R_t, R_b).$$

Computing the Model

We solve the problem of maximizing the volume using the Matlab fmincon optimization solver. A few of these optimized shapes are shown in Fig. S2B. To obtain $\frac{dV}{d\theta}$ we compute $V^*(\theta)$ and obtain the gradient with angle through a finite difference.

We note that in the actual structure there may be axial and bending loads on the robot which would affect the shape of the beam. While it may be possible to use a similar approach and parameterization of the shape to predict the response in these cases, doing so is beyond the scope of this work. In the current form, the model captures the trend and approximate magnitude of the response and is sufficient for design purposes. Another key component of the model is the ability to predict the onset of self-interference. Our model does not predict the effect of tube self-interference on joint stiffness, but it does predict when self-interference occurs.

Experimental Setup

We experimentally measure the angle and torque of the beam using the setup shown in Fig. S2C. We use 70 denier ripstop nylon fabric with a polyurethane coating to form a tube with a seam created with a line impulse sealer. The tube is secured to a frame built from aluminum extrusions by two polyoxymethylene (POM) rings. We measure the angle using a digital goniometer. We built a roller apparatus with rollers of 0.635 cm, 1.27 cm, and 2.54 cm. For all conditions the minimum distance between the rollers was 0.049 cm. We measure the force using a Mark-10 load cell rigidly attached to a POM ring sized precisely to the tube which we maintain normal to the beam. We compute the torque by multiplying the measured force by the distance from the rollers to the load cell. We control the pressure in the beam using a closed loop pressure control. We incrementally increase the angle and measure the torque, allowing time for pressure to settle to a nominal value.

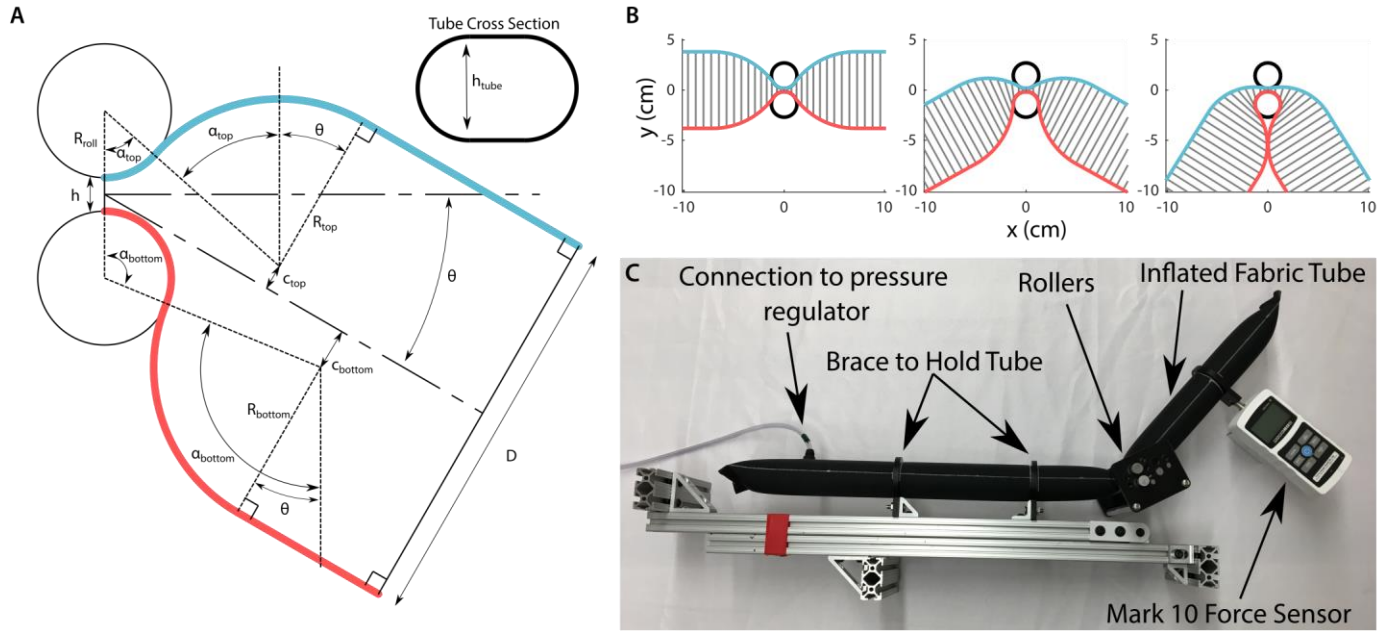

Fig. S2. (A) Parameterization of the resulting shape of the tube as it passes through the rollers. We assume

that the top and bottom path along the tube take a continuous path with two constant curvature segments. **(B)** The optimized shapes of the tube when straight, at an intermediate angle, and at the configuration where the membrane begins to self-intersect. **(C)** The test setup used to collect the data we used to compare with the model.

S3: Model Predictions of the Normal Force Between Rollers

In addition to allowing us to compute the torque required to bend to a certain angle, the same shape parameterization presented in section S2 also allows an estimation of the magnitude of the force exerted by the tube that pushes the rollers apart, which we refer to as the normal force or F_N. This force is necessary for traction yet can cause the rollers to bend. Here we define the volume as a function of the gap distance, h, and assume that the angle is specified. Using the principle of virtual work, $F_N(h,\theta) = P\frac{dV(h,\theta)}{dh}$, which allows us to quantify the force acting to separate the rollers. Fig. S3A shows the normal force as a function of the angle at different roller diameters, and Fig. S3B shows the normal force as a function of angle at different tube diameters. In general, the magnitude of the normal force decreases with angle, but overall is quite large in magnitude. In our experiments the magnitude of these forces has been sufficient to resist slipping between the tube and the rollers.

Using the normal force data from Fig. S3 we can predict the bending stress within the rollers. Assuming a normal force, $F_N = 250\ N$, that is evenly distributed along the length of the roller and that the roller is fixed at both ends, we can calculate the maximum bending stress to be:

$$\sigma_{max} = \frac{64F_N d_T}{d_R^3} = 460\ MPa$$

where the tube diameter, $d_T = 10.1\ cm$ and the roller diameter, $d_R = 1.52\ cm$. Many steels have fatigue limits in the range of $400 - 900\ MPa$ (*59*). Therefore, we can design the roller modules to be robust to cyclic loading.

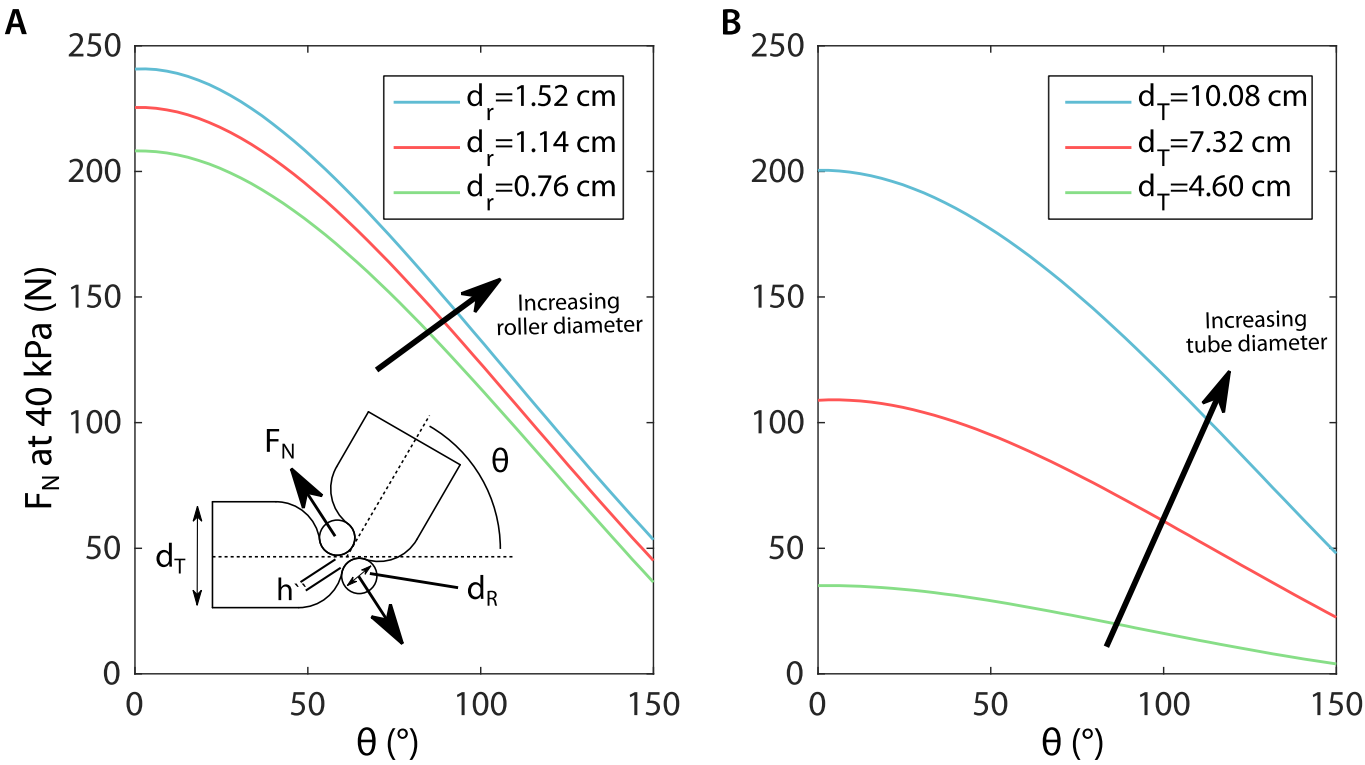

Fig. S3. (A) Model results for the normal force between two rollers at different angles and with different roller diameters. The diameter of the tube is constant at 10.08 cm. The normal force decreases with angle, and larger rollers lead to larger normal forces. **(B)** The normal force between rollers predicted by the model with different tube diameters. The rollers have a constant diameter of 0.76 cm. Increasing the tube diameter increases the normal force.

S4: Experimental Setup for Analyzing Cost to move along Rollers

The apparatus shown in Fig. S4 was used to collect the force required to move the tube with respect to the rollers. We use 70 denier ripstop nylon fabric with a polyurethane coating to form a tube with a seam created with a line impulse sealer. A series of laser cut plates held together with aluminum extrusions and standoffs locate the roller bearings and a winch system used to transmit force from a force sensor to the rollers. A pull string is connected to the Mark-10 force sensor. As the load cell is pulled, the winch system rotates one of the rollers through a belt and two pulleys. The other roller is free to spin and rotates with the driven roller because the tube presses securely against both rollers. We use three different roller diameters of 0.76 cm, 1.14 cm, and 1.52 cm. We tested three tube diameters of 4.60 cm, 7.32 cm, and 10.08 cm. For all conditions the minimum distance between the rollers was 0.049 cm. We control the pressure in the beam using a closed loop pressure control.

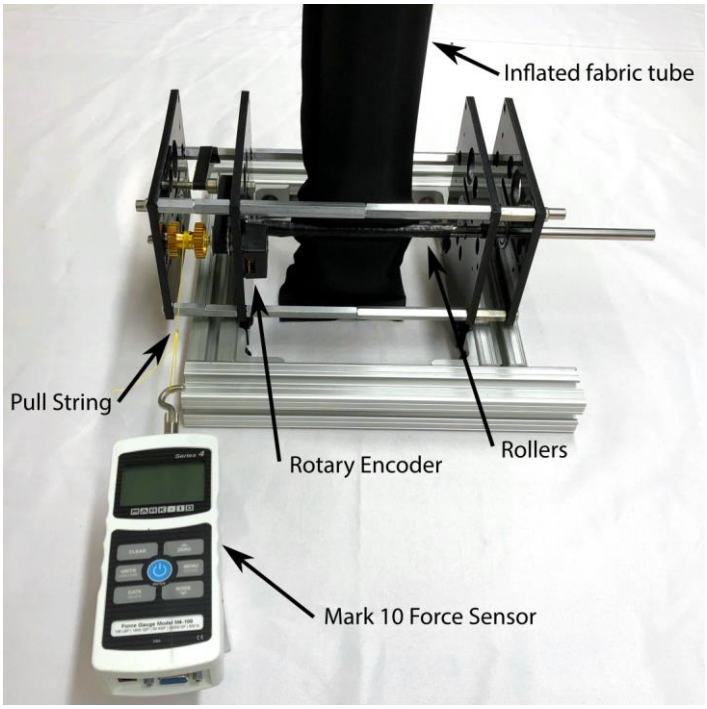

Fig. S4. Test apparatus used to measure the force required to overcome friction and move the tube through the rollers. An inflated tube was placed within the rollers and a force sensor was used to apply a torque on a shaft that was coupled to one of the rollers with a belt and pulleys. The entire length of the tube was slowly pulled through the rollers and the force required to move the rollers was averaged.

S5 Deformation of an Individual Triangle

We measure the response of a single triangle to an externally applied load using the experimental setup in Fig. S5. The passive module of the triangle is secured to a carriage free to move on a linear track. The other two roller modules are supported by a long brace and are positioned such that the linear track bisects the inner angle formed by the inflated tube at the passive module. The Mark-10 force sensor is pushed into the passive module along the linear track until the triangle completely collapses. A linear encoder tracks the position of the carriage as it moves. The Mark-10 is then moved backwards along the track as the edges of the triangle begin to straighten and exert a restoring force on the force sensor. We test three isosceles triangles: obtuse (edge lengths of 89 cm, 89 cm, and 128 cm), equilateral (edge lengths of 102 cm), and acute (edge lengths of 121 cm, 121 cm, and 64 cm). The initial pressure is set using a closed-loop pressure control and was set at 41.4 kPa. At the beginning of the test, a valve is closed such that the tests are performed with a fixed mass of air within the tube.

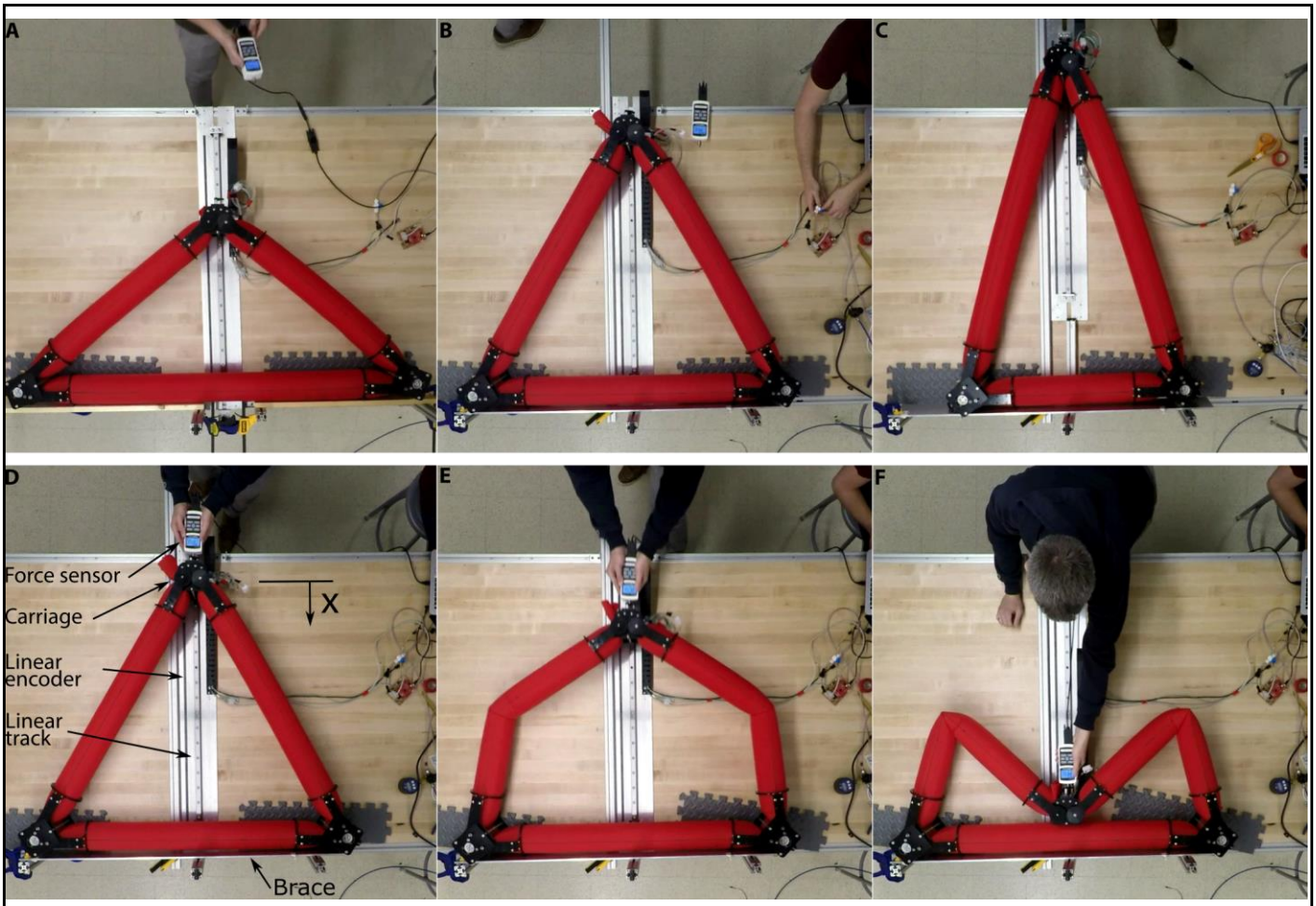

Fig. S5. Measurement of the force/displacement relationship of a single triangle. The top row of images shows three different configurations the triangle was tested in. **(A)** Obtuse triangle (edge lengths of 89 cm, 89 cm, and 128 cm). **(B)** Equilateral triangle (edge lengths of 102 cm). **(C)** Acute triangle (edge lengths of 121 cm, 121 cm, and 64 cm). The bottom row of images shows the equilateral triangle (B) being loaded. **(D)** The triangle is initially stiff to external loads. **(E)** With a sufficiently large load the triangle buckles. **(F)** The triangle at maximum displacement.

S6 Roller Module Design

A part callout of the roller module is presented in Fig. S6. The roller module is fabricated from POM sheets separated by steel hexagonal standoffs. All electronic components, as well as the node connection components are attached to the top plate of the roller module. A key structural challenge is managing the large forces required to pinch the fabric tube which are modeled in S3. While this force is supported by the

structure of the roller module itself, these forces can be extremely large and the steel rollers that we utilize bow visibly in our current system.

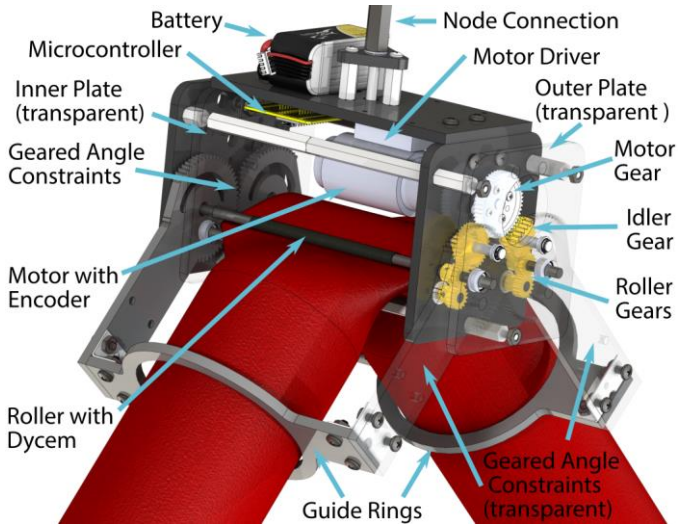

Fig. S6. Part callout of a roller module. Four parts in this figure are falsely transparent so that other parts can be shown. The outer plate on the right-hand side and the two geared angle constraints on the right-hand side are transparent so the transmission can be seen. The inner plate on the left-hand side is transparent so the geared angle constraints can be seen.

S7: Descriptive Figure for the kinematics

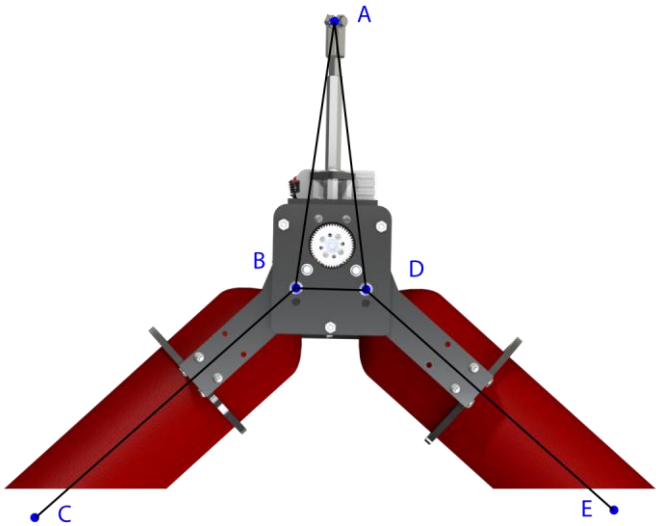

Fig. S7. An illustration of the three points at each roller module that are used to represent the state of the

robot. Point A is the connection between two roller modules. Points B and D are the center points of the rollers. Points C and E are the opposite ends of the respective edges.

S8: Comparison with other robots

In simulation we compare the efficiency and speed of an idealized isoperimetric robot and a truss robot composed of two actuators mounted at pin joints. Specifically, we compute the energy required to move Node 2 of robot A and C in Fig. 8 and Fig. S8 between a set of waypoints in a prescribed amount of time. The waypoints are randomly generated within a square region superimposed within the shared workspace of the two robots (Fig. S8A). We assume that each node is a point mass of 2.63 kg, and that the edges have no mass. We first define the motion by specifying that Node 2 move in a straight line between waypoints, following the velocity profile shown in Fig. S8B. We then utilize the kinematics presented in Materials and Methods to compute the forces and speeds required from the robot actuators to create the motion while the robot is subject to both inertial and gravitational loads. Given the torques and speeds of the actuators, we compute the total output energy for the actuators as $(\int \tau(t)\omega(t)dt)$. Fig. S8C shows that the isoperimetric robot requires slightly less energy at low frequencies, but higher amounts of energy at higher frequencies. For a prescribed motion of Node 2, Node 3 of the isoperimetric robot must also move to maintain the constant perimeter. The additional motion of Node 3 is increasingly costly as frequency increases and dynamic effects become more pronounced.

We also compare the efficiency and speed for different power sources. Given the speed and torques required from the actuators, we can determine the amount of energy that must be input to the system given an actuator choice of a specific motor or microcompressor. We compute the input power as $(\int V(t)i(t)dt)$ for either the motor or the microcompressor. As our representative motor we select the Actobotics 52 RPM (#638296) premium planetary gear motor (231.22:1 gear ratio, mass of 118 g). For the microcompressor we select the Parker Hargraves BTC-IIS microcompressor (170 g) due to its characterization in past studies and its similar weight to the motor (*40*). In the case of the microcompressor, we must relate the linear motion and force of the pneumatic cylinder to the pressure and flow rate at the microcompressor. We assume that the piston has constant diameter such that $PA = F$.
Examining the closed volume within the cylinder and assuming an isothermal process, we write the following

$$PV = mRT$$
$$\dot{P}V + P\dot{V} = \dot{m}RT$$
$$\dot{m} = \frac{1}{RT}\left(\frac{dF}{dt}L + P_g + P_{atm}\dot{L}A\right)$$

This allows us to compute the flow rate required at the microcompressor given a time history of pressure and length of the actuator, which together with the microcompressor parameters allows us to compute the input energy.

We compare the required input energy to move the robot between waypoints. We compare robot A in Fig. 8 with two different types of robot C: one of linear actuators driven by motors and one of pneumatic cylinders driven by microcompressors (Fig. S8D). Across all of the time scales studied, the input power required by the isoperimetric robot is higher than for the motor-driven robot composed of linear actuators. Both motor driven systems complete the trajectories in a minimum time of 11 seconds, while the microcompressor-based system takes 273 seconds to complete the trajectory. We note that the energy required increases faster for the

motor driven system then for the microcontrollers, such that the energy required switches at low speeds. This is because at slow speeds the motors are far from operating at their most efficient condition. We also note that for the idealized motor-driven system where the motors are perfectly backdrivable, the motors must exert a holding torque to keep the end effector at rest. For the pneumatic system, no energy is required to hold the system at a stationary condition. These results indicate that the motor driven system has the potential for faster and more efficient operation at moderate speed scales.

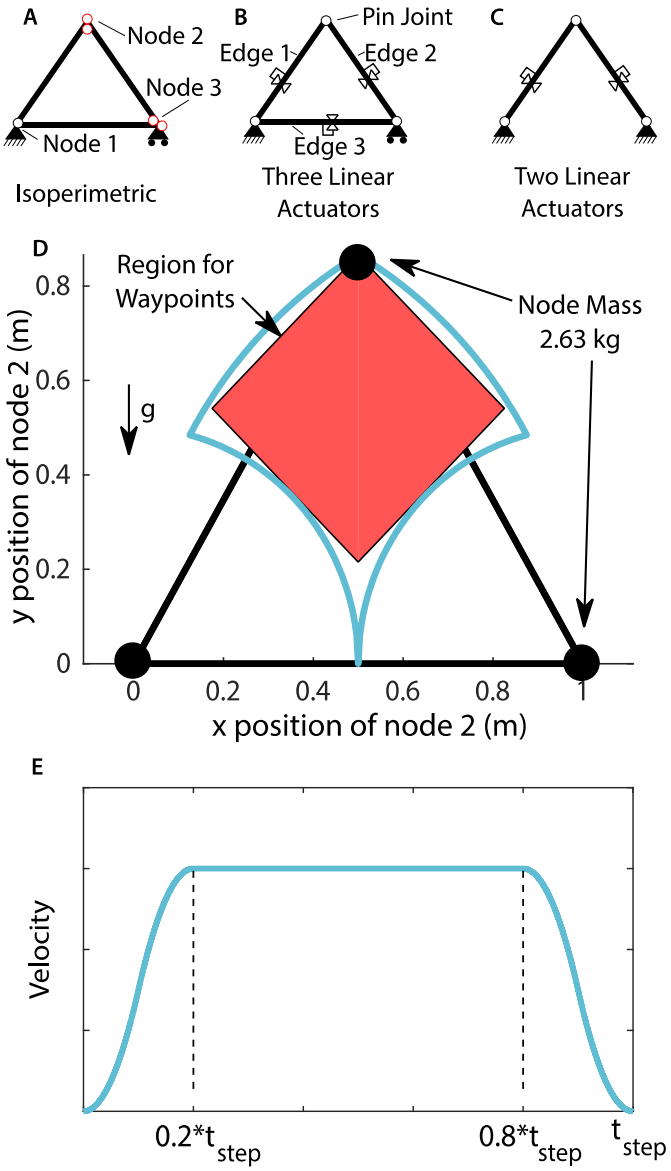

Fig. S8. Comparison of the robots' energy required to move between randomly generated waypoints. **(A)**

The robot moves the Node 2 to waypoints that are randomly generated within the square superimposed

within the shared workspace of the robots. The node moves in a linear path between the waypoints

seconds according to the velocity profile shown in **(B)**.

Movie S1 - Motion of the roller module along an inflated tube
This movie shows close-up shots of the roller module. The first segment shows how the rollers drive along the inflated tube like wheels. The camera is fixed with respect to the roller modules. As the motor drives the rollers, the striped tube appears to move through the rollers. In the second segment the roller module moves along an inflated tube that is pinned to the ground at its ends and forms a triangle. The camera is fixed with respect to the ground. As the roller module moves, the shape of the triangle changes as one edge shortens and the other lengthens. In the final segment, we see how the guide rings are constrained to move together due to the geared angle constraints.

Movie S2 - Inflation and shape change of a 2D robot
A 2D robot composed of three separate inflated tubes is demonstrated in this movie. The inflated tubes are formed into triangles with two active roller modules and one passive module. The triangles are then connected to each other to form this robot. The robot is initially deflated and inflates into an equilateral triangular shape. After the operating pressure is reached, the robot is untethered from the external compressor. At this point the roller modules move along the inflated structure to change the shape into an obtuse triangle, hexagon, acute triangle, square, and a pincer that can grasp a basketball.

Movie S3 - Operation of a single tube 2D robot
A 2D robot composed of just a single inflated tube is demonstrated in this movie. To shorten and lengthen the two edges adjacent to an active roller module, that active roller module simply drives along the tube. To change the adjacent edge lengths of the passive module with a similar connectivity, all of the active roller modules in the network must drive to preserve the other edge lengths. With this network, there is only a single length constraint for the entire network and any two edges can trade length. In this movie we also see how we can make some edges extremely long by reducing the length of other edges in the network.

Movie S4 - Shape change of octahedron robot
This movie demonstrates the octahedron robot changing shape in interesting ways despite the constant length constraints. The first segment shows how the structure can twist. The second segment shows the structure growing tall, spreading flat and short, and extending one of its nodes out to the side. As the robot moves from one configuration to the next, the structure takes some unintuitive intermediate shapes due to the unique construction of this robot. In general, edges connecting two active roller modules can change length twice as fast as edges connecting a passive module and an active roller module.

Movie S5 - Comparison of predicted and measured motion
This movie conceptually compares the observed motion of the robot to the predicted motions from the kinematic simulation. The commands used as inputs to the simulation are the same commands that were sent to the robot in the experiment, and we assume that each roller module moves along the tube at a constant speed. While the simulation does not account for the deflection and dynamic motions that occur in the actual experiments, it does capture the character of the movement.

Movie S6 - Octahedron robot locomotes with a punctuated rolling gait
This movie demonstrates a 3D robot constructed with the same roller modules used for the 2D demonstrations. Four separate inflated tubes are formed into triangles with two active roller modules and one passive module. The four triangles are then connected together to form an octahedron structure with planar faces. The shape of the structure changes as the roller modules drive along the inflated tubes. This shape change enables locomotion of the robot with a punctuated rolling gait. The same demonstration was filmed from two perspectives. We also show the robot locomoting while untethered in an outdoor environment.

Movie S7 - Compliance and interaction of the robot with people
This movie demonstrates the inherent compliance of the robot as it interacts with people. In the first movie a user applies loads by pushing on the robot. Under all loads, the structure exhibits some softness due to the compliant nature of the beams. If the user applies a large force on the beam, the inflated beams will buckle, reducing the force required by the user to maintain a given level of deflection. This gives the structure a behavior similar to that of a mechanical fuse. When the load is released from a buckled configuration the robot will occasionally recover to the nominal configuration on its own but will sometimes require an external load to return to the nominal configuration. The robustness of the robot is demonstrated as no permanent damage is caused by this buckling. In the second movie two users interact with the robot by carrying it, rolling it around, causing it to buckle, climbing

inside the robot, and standing on some of the edges of the robot that are on the ground while the robot is in operation.

Movie S8 - Octahedron robot moving a payload
In this movie the octahedron robot moves back and forth while two metal plates with a mass of 6.8 kg are attached to the joint between two roller modules. This demonstrates the ability of the robot to apply large forces. Due to the parallel structure of the robot, in this case two different motors contribute to moving the mass.

Movie S9 - Simulated Loading with payload
This movie shows a simulation of the octahedron robot moving back and forth while a 66.7 N load (indicated by the arrow) is applied at one of the connections between roller modules. Also included in the load is the weight of each roller module. The color of each edge corresponds to the loading condition, where negative values for the axial forces correspond to compressive loads. The kinematics presented in the materials and methods section are used to compute the Jacobian, which is used to simulate the motion from actuator inputs, as well as reconstruct the axial loads on the edges under the given loading condition. These results are for a quasi-static case, meaning there are no dynamic effects.

Movie S10 - Self-recovery from buckling
This movie illustrates two different strategies that allow the octahedron robot to recover from a buckled configuration. In the first case, a roller module connected to the buckled edge moves towards the buckle point, eventually straightening the beam as the buckle point enters the roller module. In the second case, we move the other roller modules in the network to reduce the load on the buckled edge, allowing the restoring forces within that buckled beam to straighten that edge.

Movie S11 - Manipulation
This movie illustrates the robot using the inherent compliance to interact with objects. First the robot grasps a basketball by moving over it to engulf it, pinching it between two of the inflated beams, and then changing shape to lift the basketball. Second, the movie shows that when a basketball is placed between two beams, motion of the roller modules can cause the basketball to rotate while the grasp is maintained. Third, a bucket of ball is handed off to the robot, which then changes shape to dump out the bucket.

Movie S12 - Reachable workspace for a single triangle
This movie illustrates the theoretical workspace of the top node of a triangle robot built from a single tube using our concept. The top node traces the boundary of the workspace. The tube is of length 3 units, and the minimum allowable edge length is .5 units. The bottom left node of the triangle is fixed, and the bottom right node of the triangle is fixed in the vertical but not the horizontal direction.